INFORMATION COMPLÉMENTAIRE RELATIVE À LA RECONSTITUTION DE SÉRIES HISTORIQUES DE PRODUCTION ÉOLIENNE ET À LA CONTRIBUTION EN PUISSANCE DES PARCS ÉOLIENS

TABLE DES MATIÈRES

Comme mentionné à la pièce HQD-1, document 2 du présent dossier et en conformité avec la décision D-2019-041, le Distributeur dépose les informations relatives à la reconstitution de séries historiques de production éolienne ainsi que la mise à jour de l'évaluation de la contribution en puissance des éoliennes qui en découle.

Sur la base des séries historiques de production éolienne, le Distributeur souhaite proposer un profil alternatif pour les retours d'énergie aux soumissionnaires participant à l'appel d'offres en vue de l'acquisition du service d'intégration éolienne.

1. RECONSTITUTIONS DE SÉRIES HISTORIQUES DE PRODUCTION ÉOLIENNE

Le Distributeur a octroyé un mandat de reconstitution de séries historiques de production éolienne à la firme AWS Truepower (AWS). Les résultats de ce mandat sont présentés dans le rapport *Historical Meteorological and Wind Power Time Series 1979-2015,* déposé à l'annexe A de la présente pièce.

Les principaux objectifs du mandat étaient de reconstituer un historique des données météorologiques pour l'ensemble des parcs éoliens sous contrat avec le Distributeur et, à partir de ces données, de produire des séries historiques de la production nette[1] d'énergie éolienne. AWS a ainsi simulé la production éolienne à l'emplacement des 39 parcs éoliens, tels que connus en date de l'étude, en utilisant des données météorologiques historiques couvrant la période de janvier 1979 à décembre 2015.

La production d'énergie anticipée à partir des simulations a permis d'obtenir des séries horaires de production pour la période couverte, et ce, pour chacun des parcs éoliens étudiés.

2. ÉVALUATION DE LA CONTRIBUTION EN PUISSANCE À LA POINTE DES ÉOLIENNES

À partir des données de reconstitution historique de la production éolienne de la firme AWS, le Distributeur a mis à jour l'évaluation de la contribution en puissance à la pointe des éoliennes. Le rapport détaillé est déposé à l'annexe B.

L'analyse réalisée avec le modèle de fiabilité MARS consiste à calculer l'apport en puissance des éoliennes à la pointe, en tenant compte de leur contribution pour assurer le respect du critère en fiabilité du NPCC auquel le Distributeur doit se conformer, soit une espérance de délestage n'excédant pas 0,1 jour par année.

Sur la base des résultats obtenus, le Distributeur révise ainsi la contribution en puissance à la pointe des éoliennes à 36 % de la puissance éolienne installée.

[1] Tenant compte des pertes diverses dues par exemple au sillage, aux conditions météorologiques extrêmes ou encore aux pertes électriques.

3. AJOUT D'UN PROFIL DE RETOURS D'ÉNERGIE

Au présent dossier, le Distributeur a reconduit les retours d'énergie du service d'intégration éolien (SIÉ) actuel, soit des retours à hauteur de 40 % de la puissance éolienne installée pour les mois d'octobre à mars et de 30 % pour les autres moins de l'année. Sur une base annuelle, les retours d'énergie assurent ainsi un volume d'énergie de 35 % de la puissance installée, ce qui correspond à la production en énergie éolienne attendue et aux paramètres des contrats intervenus avec les fournisseurs éoliens.

Tout en maintenant ce profil de retours d'énergie pour l'appel d'offres à lancer, le Distributeur propose d'ajouter un deuxième profil de retours d'énergie possible. En effet, sur la base des séries reconstituées de production éolienne produites par la firme AWS, dont le profil mensuel est présenté à la section 2.2 du rapport d'évaluation de la contribution en puissance de la production éolienne (annexe B), un profil en trois niveaux différents a été établi, soit :

- 42,5 % pour les mois de décembre à mars ;
- 25 % pour les mois de juin, juillet et août ;
- 35 % pour les autres mois, soit avril et mai ainsi que septembre à novembre.

Le profil proposé assurerait également un volume annuel d'énergie correspondant à 35 % de la puissance éolienne installée. Il permettrait toutefois d'accroître le niveau des retours d'énergie en hiver, et ce, en lien avec la production attendue calculée à partir des séries produites par AWS, qui est de 42,7 % de la puissance éolienne installée, pour les mois de décembre à mars.

En hiver, si ce profil était retenu, la garantie de puissance associée au SIÉ atteindrait ainsi 42,5 % de la puissance éolienne installée.

À l'issue de l'appel d'offres, le Distributeur évaluera les offres reçues pour les deux options de profil de retours d'énergie en tenant compte de leurs impacts respectifs sur les coûts totaux d'approvisionnement.

ANNEXE A :

RAPPORT DE AWS TRUEPOWER

HISTORICAL METEOROLOGICAL AND WIND POWER TIME SERIES 1979-2015

AWS Truepower®

PREPARED FOR:
HYDRO-QUEBEC DISTRIBUTION

HISTORICAL METEOROLOGICAL AND WIND POWER TIME SERIES 1979-2015

DECEMBER 15, 2016

PROJECT NUMBER: 16-00336

QUEBEC, CANADA

CLASSIFICATION
Public version
Report Issue
D

463 NEW KARNER ROAD | ALBANY, NY 12205
awstruepower.com | info@awstruepower.com

NOTICE TO THIRD PARTIES

This report was prepared by AWS Truepower, LLC (AWS Truepower) and is based on information not within the control of AWS Truepower. AWS Truepower has assumed the information provided by others, both verbal and written, is complete and correct. While it is believed the information, data, and opinions contained herein will be reliable under the conditions and subject to the limitations set forth herein, AWS Truepower does not guarantee the accuracy thereof. Use of this report or any information contained therein by any party other than the intended recipient or its affiliates, shall constitute a waiver and release by such third party of AWS Truepower from and against all claims and liability, including, but not limited to, liability for special, incidental, indirect, or consequential damages in connection with such use. In addition, use of this report or any information contained herein by any party other than the intended recipient or its affiliates, shall constitute agreement by such third party to defend and indemnify AWS Truepower from and against any claims and liability, including, but not limited to, liability for special, incidental, indirect, or consequential damages in connection with such use. To the fullest extent permitted by law, such waiver and release and indemnification shall apply notwithstanding the negligence, strict liability, fault, breach of warranty, or breach of contract of AWS Truepower. The benefit of such releases, waivers, or limitations of liability shall extend to the related companies and subcontractors of any tier of AWS Truepower, and the directors, officers, partners, employees, and agents of all released or indemnified parties.

KEY TO DOCUMENT CLASSIFICATION

STRICTLY CONFIDENTIAL	For recipients only
CONFIDENTIAL	May be shared within client's organization
AWS TRUEPOWER ONLY	Not to be distributed outside AWS Truepower
CLIENT'S DISCRETION	Distribution at the client's discretion
FOR PUBLIC RELEASE	No restriction

DOCUMENT CONTRIBUTORS

AUTHOR(S)	REVIEWER(S)
Beaucage, Philippe Kramak, Brian Shakarjian, Mikel	Brower, Michael Robinson, Nick

TABLE OF CONTENTS

LIST OF FIGURES

LIST OF TABLES

EXECUTIVE SUMMARY

On behalf of Hydro-Québec Distribution (HQD), AWS Truepower (AWST) created historical wind power generation and associated plant losses for the period of 1979 – 2015. The goal was to provide realistic meteorological and wind power generation time series that mimicked the operational behaviors of the 39 wind plants in Québec under HQD contract. The Weather Research and Forecasting (WRF) model, an open-source numerical weather prediction model, was used to generate the meteorological variables necessary to simulate wind energy production. The simulated wind speeds were downscaled with the WindMap microscale model. The conversion of the meteorological time series into wind power generation was performed by the Openwind software. Improvements in modeling time-varying plant losses allowed the Openwind software to simulate a wind plant as a fully dynamic system reporting wind power generation and individual plant losses on an hourly basis. Twelve different wind turbine models from five different original equipment manufacturers (OEM) were incorporated into Openwind. The categories of plant losses included: wake, availability, environmental, electrical and turbine performance.

The modeled net power generation was compared to actual (observed) generation at each 18 operational wind farm. The validation of the WRF-WindMap-Openwind simulations indicated that the net wind power generation was well aligned with the actual generation where the average hourly coefficient of determination (R^2) was 0.80, while the mean daily R^2 was 0.88. Our analyses also indicated that the monthly/seasonal trends in net power are well captured by the simulation system. The long-term average plant losses at each wind farm over the entire 37-year period are summarized in the report. A direct comparison between modeled and observed plant losses was not possible for this effort as most plant losses such as wakes and turbine performance are not easily derived from operational wind turbine data obtained through the SCADA system. Therefore, AWST's validation focused on the availability and icing losses which provided a reasonable approximation of the observed losses, although icing losses remain challenging at any given site. Power consumption losses, due to the rotor blade heating systems, were also a focal point. This report presents an overview of the methods, results, and validation of the historical wind power generation and associated plant losses at 39 wind farms in Québec.

1. INTRODUCTION

Electrical grids with a high penetration of wind generation face challenges characterizing the spatial and temporal variability of the wind resource and its effect on the reliability of the grid. Understanding and predicting the wind resource and resulting power generation, especially during periods of high electrical demand – winter season in Québec, is critical for grid operations to ensure system stability and cost effectiveness as well as addressing sensitivities to operating reserves, storage options, market scenarios, carbon reduction plans, etc.

AWS Truepower (AWST) was retained by Hydro-Québec Distribution (HQD) to develop a historical simulation of wind power generation and associated losses for the period of 1979 – 2015. The goal was to provide realistic meteorological and wind power generation time series that mimicked the operational behaviors of the 39 wind plants in Québec under HQD contract.

1.1 Project Goals

- Create atmospheric and wind power generation time series at 39 wind plants in the Québec project area for the period of 1979 – 2015.
- Incorporate the historical records from the meteorological towers and supervisory control and data acquisition (SCADA) system at the operational plants to refine and improve the modeling used to simulate power generation.
- Refine and validate the conversion of meteorological conditions into net energy production at the plants, accounting for several types of energy losses: wakes, availability, environmental (low and high temperature shutdowns, high wind hysteresis, icing), turbine performance and electrical losses (electrical efficiency and turbine power consumption). Particular attention focused on icing-related losses in order to properly simulate the wind power generation during the cold season.

1.2 Project Overview

This report is divided into three main sections and provides an overview of the methods used to simulate meterological conditions as well as wind power generation and associated plant losses at 18 operational and 21 non-operational wind farms in Québec for the 1979 – 2015 period.

Section 2 of this report describes the data sets acquired from HQD, as well as the quality control process used by AWST. HQD provided temporary met mast (TMM) or pre-construction met mast data for all 39 wind plants. The highest quality TMMs were identified and the met mast data was quality controlled for completeness and reasonableness. HQD also provided 10-minute operational data from the turbine SCADA system at the 18 operational wind farms.

Section 3 summarizes the methods used to develop the modeled atmospheric time series using a state-of-the-art NWP model, WRF. The 3-km horizontal resolution WRF simulations were evaluated against TMM data to determine the accuracy of several meteorological variables, and then downscaled with the WindMap microscale model to reach finer spatial resolution and achieve higher accuracy.

Section 4 describes the transformation of the meteorological time series into wind power generation using Openwind, a state-of-the-art wind resource assessment and layout optimization software. The Openwind simulations first converted the meteorological time series into gross wind power production or the theoretical amount of power a wind turbine or a wind farm would produce assuming no wind plant losses. Then, the net energy production is derived by subtracting all the wind plant losses from the gross energy. AWST made several adjustments to the time-varying plant loss modules in the Openwind software which are described in this section. Twelve different wind turbine models from five different original equipment manufacturers (OEM) were incorporated into Openwind.

The observed energy losses from the turbine's SCADA system were used to verify the Openwind model and confirm that it reproduces the observed plant behavior with sufficient fidelity. After achieving satisfactory validation results at the operational wind farms, the Openwind simulations were run for the entire 1979 – 2015 study period. By relying on WRF, WindMap and Openwind, AWST estimated gross production, net production and the following losses at all 39 plants: wake, availability, environmental (low and high temperature shutdowns, high wind hysteresis, icing), turbine performance and electrical losses (electrical efficiency and turbine power consumption). A detailed description of the power conversion process can be found in Section 4.

2. ATMOSPHERIC AND PLANT DATA ACQUISITION

The wind farm developers and owners/operators, via HQD, provided pre-construction met mast data at existing or planned wind farms under contract with HQD. HQD also provided operational plant data from the turbine supervisory control and acquisition (SCADA) system at the 18 operating wind farms.[2.1] Additional data provided by HQD included wind farm layouts, turbine characteristics, such as power and thrust curves, documentation about the cold weather packages, icing operation modes, blade heating systems, storm control systems for high winds, etc. Table 2.1 provides a brief summary of wind plant characteristics.

Table 2.1: Plant characteristics for the 39 wind farms under contract with HQD

Plant ID	Plant Status	Turbine OEM and model	Blade Heating System
P1	Operational	GE 1.5 sle, 1.5 MW	No
P2	Operational	GE 1.5 sle, 1.5 MW	No
P3	Operational	GE 1.5 sle, 1.5 MW	No
P4	Non-operational	Enercon E-92, 2.35 MW	Yes
P5	Non-operational	Senvion MM92, 2.05 MW	No
P6	Operational	Enercon E-82 E2, 2.05 MW	Yes
P7	Non-operational	Enercon E-92, 2.35 MW	Yes
P8	Operational	Enercon E-82 E2, 2.35 MW	Yes
P9	Non-operational	Enercon E-82 E2, 2.05 MW	Yes
P10	Operational	GE 1.5 sle, 1.5 MW	No
P11	Operational	Senvion MM82, 2.05 MW (33) and MM92, 2.05 MW (117)	No
P12	Non-operational	Senvion MM92, 2.05 MW	No
P13	Non-operational	Enercon E-92, 2.35 MW	Yes
P14	Operational	Enercon E-70 E4, 2.31 MW	Yes

[2.1] As of December 2015

Plant ID	Plant Status	Turbine OEM and model	Blade Heating System
P15	Operational	Senvion MM82, 2.05 MW (31) and MM92, 2.05 MW (44)	No
P16	Operational	GE 1.5 sle, 1 MW	No
P17	Non-operational	Senvion MM92, 2.0 MW	Yes
P18	Operational	GE 1.5 sle, 1.5 MW	No
P19	Non-operational	Siemens SWT 3.2-113, 3.2 MW	No
P20	Non-operational	Senvion MM92, 2.05 MW (1) and 3.2M114, 3.2 MW (46)	Yes
P21	Non-operational	Vestas V117, 3.3 MW	Yes
P22	Operational	Enercon E-82 (27 x 2.05 MW and 6 x 2.35 MW)	Yes
P23	Non-operational	Senvion MM92, 2.05 MW	No
P24	Non-operational	Senvion MM82, 2.05 MW (85) and MM92, 2.05 MW (90)	No
P25	Non-operational	GE 2.2-107, 2.2 MW	No
P26	Operational	Enercon E-70 E4, 2.31 MW (24) and E-82 E2, 2.35 MW (38)	Yes
P27	Operational	Enercon E-70 E4, 2.31 MW (42) and E-82 E2, 2.35 MW (22)	Yes
P28	Non-operational	Enercon E-82 E2, 2.35 MW (23) and E-82 E4, 3.0 MW (5)	Yes
P29	Non-operational	Enercon E-92, 2.35 MW	Yes
P30	Non-operational	Enercon E-92, 2.35 MW	Yes
P31	Non-operational	Enercon E82 E4, 3.0 MW	Yes
P32	Operational	Senvion MM92, 2.05 MW	No
P33	Operational	Enercon E-82 E2, 2.35 MW	Yes

Plant ID	Plant Status	Turbine OEM and model	Blade Heating System
P34	Operational	GE 1.5 sle, 1.5 MW	No
P35	Non-operational	Enercon E-92, 2.35 MW	Yes
P36	Non-operational	Enercon E-92, 2.35 MW	Yes
P37	Operational	Senvion MM92, 2.05 MW	No
P38	Non-operational	Enercon E-92, 2.35 MW	Yes
P39	Non-operational	Enercon E-92, 2.35 MW	Yes

2.1 Pre-Construction Meteorological Data at Operational and Non-Operational Wind Plants

The pre-construction met mast data (TMM) was provided by HQD on a 10-minute time interval. After reviewing the TMM dataset, AWST deemed necessary to quality control the observed data. A site investigation was carried to make sure that the wind farm layouts did not include any mistakes. Topographic maps and aerial imagery were used to confirm the location of the wind turbines. Once the data has been converted to a standard file format, a visual inspection of data was performed with the Windographer software to help diagnose boom orientation or vane shift issues, anemometer degradation as well as sensor failures.[2.2]

The quality control of the met mast data can be a tedious task because parts of the process require manual inspections. Given the lengthy process and the fact that the TMM data gathered by each wind developer was in different file formats, AWST decided to limit the number of TMM processed for each wind farm in order to meet the project's deadline. At least one TMM was processed for each non-operational wind farms. AWST's rule of thumb was to quality control one additional TMM for every 100 MW increase in plant capacity. As shown in Table 2.2, a total of 23 TMMs scattered throughout 16 different wind farms in Québec were selected by AWST. Although there are 21 non-operational wind farms under contract with HQD, 5 non-operational wind farms did not have their own pre-construction met mast data, but were located sufficiently close to an existing wind farm.

Table 2.2: Data recovery at 23 pre-construction met masts

Site Name	Start Date	End Date	Data Recovery (%)
M1	2013-10-17	2014-12-14	54
M2	2004-08-21	2014-12-31	66

[2.2] https://www.awstruepower.com/products/software/windographer/

Table 2.2: Data recovery at 23 pre-construction met masts

Site Name	Start Date	End Date	Data Recovery (%)
M3	2012-03-30	2014-11-01	53
M4	2006-10-18	2014-11-07	63
M5	2013-11-01	2014-11-07	76
M6	2011-09-09	2014-03-24	56
M7	2012-03-13	2014-12-31	52
M8	2012-07-12	2014-07-01	91
M9	2012-09-03	2014-07-01	88
M10	2014-02-02	2014-07-01	74
M11	2009-09-01	2013-08-31	89
M12	2013-09-19	2014-09-29	56
M13	2013-07-30	2014-09-29	51
M14	2013-08-24	2014-09-29	52
M15	2013-12-23	2014-11-30	46
M16	2009-09-03	2012-06-14	65
M17	2012-07-21	2014-01-23	59
M18	2006-06-07	2009-08-04	38
M19	2012-08-01	2014-12-31	57
M20	2012-08-01	2014-09-08	65
M21	2013-12-17	2014-10-14	75
M22	2013-12-18	2013-12-21	70
M23	2006-03-23	2014-12-31	66
Average	-	-	**63**

2.2 SCADA Data at Operational Wind Farms

The SCADA data for each operational wind farm were provided in a standardize file format with five CSV files per wind farm. At the turbine level, the nacelle anemometer and wind vane measurements, power generation and status code were included. At the plant level, the files included the number of turbines shutdown under different environmental categories (low or high temperatures, low or high winds, icing), power station availability, net metered production at the substation, etc.

The number of records by year and month is shown in Table 2.3 for each operational wind farm, up to December 2015, when the data was provided for the study. The table below shows the start year and month when HQD and AWST estimated that the SCADA data was free from the shakedown effects which is typically 4 months (or more) after the commercial operation date. In other words, Table 2.3 shows the amount of valid SCADA data.

Table 2.3: Number of records by year and month at each 18 operational wind farm. The values correspond to the number of valid hourly records in each month. The color gradient from red (low), to yellow and green (high) reflects the number of records.

SITE	Year	Jan	Feb	Mar	Apr	May	June	July	Aug	Sept	Oct	Nov	Dec
P1	2008			744	720	744	720	733	744	720	744	720	744
	2009	744	672	744	720	744	720	744	731	720	744	720	636
	2010	744	672	744	720	744	720	744	742	720	744	720	744
	2011	744	672	744	720	744	720	744	744	720	744	720	744
	2012	744	696	744	720	744	720	744	744	720	744	720	744
	2013	744	672	744	720	744	720	744	744	720	744	720	744
	2014	744	672	744	719	744	720	733	744	713	744	720	744
	2015	744	672	744	720	744	720	734	743	720	744	720	744
P2	2008	738	696	744	720	738	650	744	744	720	725	712	744
	2009	744	672	744	696	744	720	687	744	720	744	720	744
	2010	744	672	744	720	744	720	744	744	720	744	720	744
	2011	744	672	744	720	743	720	744	744	720	744	720	744
	2012	744	696	744	720	744	720	744	744	720	744	720	744
	2013	744	672	744	720	744	720	744	744	720	744	720	744
	2014	744	672	744	720	744	720	744	744	693	744	720	744
	2015	744	672	744	720	744	720	744	744	708	744	720	744
P3	2009			744	720	744	720	744	744	720	744	720	719
	2010	744	672	744	720	744	720	732	744	720	744	720	744
	2011	744	672	744	720	744	720	744	744	720	744	720	744
	2012	744	696	744	720	744	720	744	744	720	744	720	744
	2013	744	672	713	703	744	720	733	721	691	744	720	744
	2014	715	672	744	720	744	720	744	744	720	744	720	744
	2015	744	672	744	720	744	720	744	744	720	744	720	743
P6	2014			744	712	744	720	732	744	720	744	720	744
	2015	744	660	735	720	744	720	654	744	720	744	720	744

SITE	Year	Jan	Feb	Mar	Apr	May	June	July	Aug	Sept	Oct	Nov	Dec
P8	2014				720	744	691	744	744	720	744	720	743
	2015	664	672	744	720	744	720	744	718	720	744	720	744
P10	2013			715	687	696	702	681	710	708	697	700	738
	2014	741	668	732	686	675	675	731	605	695	700	699	741
	2015	730	668	736	700	713	650	692	732	704	705	704	710
P11	2014			744	720	744	720	707	744	720	744	720	744
	2015	744	672	744	720	744	705	742	740	720	744	720	744
P14	2012							744	740	615	744	720	744
	2013	744	672	744	719	688	719	741	744	720	744	720	744
	2014	744	672	744	720	744	720	744	639	716	744	711	741
	2015	744	672	744	720	741	710	744	744	720	744	720	744
P15	2014			744	720	744	720	744	587	720	744	707	744
	2015	723	672	740	710	744	720	644	744	720	744	713	744
P16	2012	734	692	740	519	744	637	732	434	518	686	713	664
	2013	710	672	744	720	744	720	736	708	720	744	720	744
	2014	702	672	744	706	744	720	744	680	720	744	720	744
	2015	744	672	744	720	744	720	721	744	720	744	720	744
P18	2012			744	720	744	705	744	744	704	744	720	744
	2013	744	559	671	656	634	678	664	676	694	665	673	694
	2014	711	649	734	670	631	592	628	586	675	685	672	650
	2015	714	626	709	683	689	616	619	636	684	651	680	639
P22	2013							636	744	711	742	720	744
	2014	744	672	740	720	744	719	582	744	720	734	720	737
	2015	744	672	744	720	744	720	702	744	720	744	715	744
P26	2014			744	720	744	678	744	744	720	742	720	744
	2015	744	672	744	720	744	719	744	729	720	744	720	744
P27	2014				720	744	678	744	738	720	744	720	744
	2015	744	672	744	720	744	719	744	729	720	744	720	744
P32	2014			744	720	495	720	717	744	720	741	720	738
	2015	744	672	743	720	651	719	740	743	720	736	720	744
P33	2013				720	744	720	744	744	709	744	720	744
	2014	744	672	744	713	743	720	744	716	707	744	720	744
	2015	744	672	742	615	743	720	744	744	720	744	720	744
P34	2010			744	720	744	720	709	744	720	744	720	744
	2011	744	672	744	720	744	720	744	744	674	744	478	710
	2012	744	696	744	720	744	720	744	744	720	744	720	744
	2013	744	672	744	720	744	720	744	738	720	744	720	738
	2014	744	672	744	720	744	720	744	744	720	744	720	744
	2015	744	672	744	720	744	720	744	673	717	744	720	744
P37	2014			744	719	730	717	744	707	720	737	716	744
	2015	744	672	744	720	744	720	718	741	720	744	720	744

3. MODELED ATMOSPHERIC TIME SERIES

Modeling the non-linear, non-stationary atmospheric circulations is challenging. Mesoscale numerical weather prediction (NWP) models – the same models used for weather forecasting – are the best tools available to simulate the evolving atmospheric conditions, especially the synoptic scale and mesoscale. For this project, AWST relied on the state-of-the-art NWP model, the Weather Research and Forecasting (WRF) model. WRF is an open-source model developed by NCAR, NOAA (NCEP), AFWA, Naval Research Lab, University of Oklahoma and FAA in the early 2000s. Based on WRF simulations, AWST created hourly meteorological time series for each HQD plant for the 1979 to 2015 period.

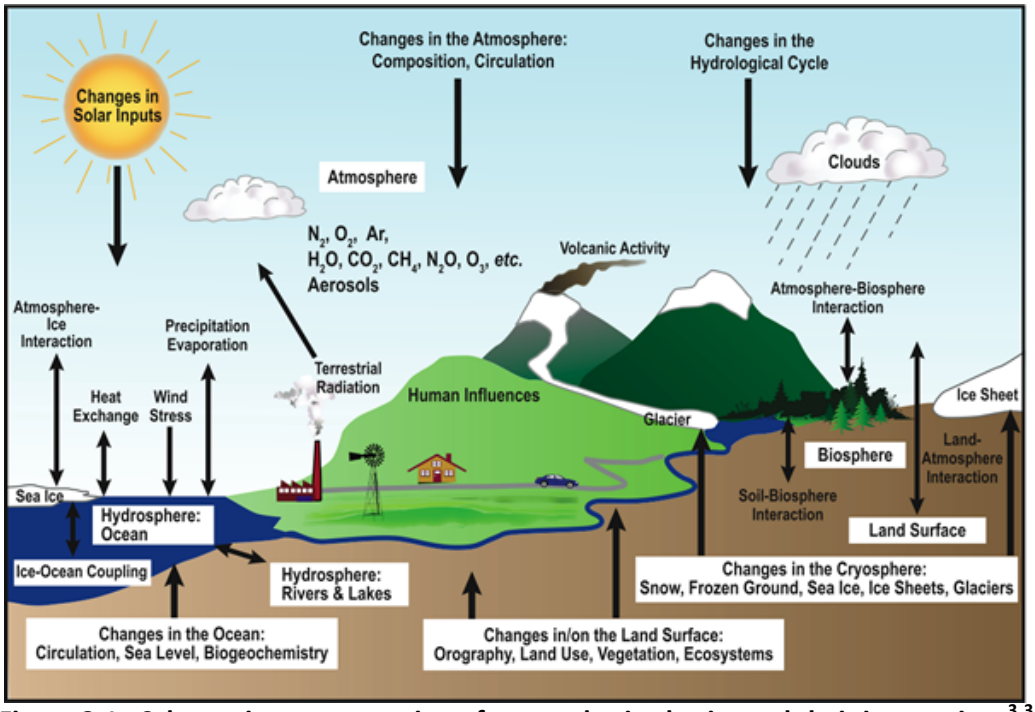

Figure 3.1: Schematic representation of atmospheric physics and their interactions[3.3]

WRF solves the fully compressible, non-hydrostatic Navier-Stokes equations (i.e. conservation of mass, momentum and energy) and includes a complete suite of physics parameterization schemes, including radiation, land surface-atmosphere interactions, planetary boundary layer (PBL) turbulence, microphysics, cloud convection (Figure 3.1). WRF contains 11 boundary layer schemes, 18 microphysics schemes, and 10 convective parameterization schemes and a three-dimensional (3D) grid to simulate atmospheric processes. The 3D grid can cover a large area, sometimes a province/state, a country or the globe depending on the grid resolution; a coarser grid can cover a larger area with the same number of grid cells. The vertical levels of NWP models extend far into the stratosphere, typically up to 50 mb, which is roughly equivalent to 20.5 km in altitude, in order to capture the jet stream. An example of such a 3D grid is shown in (Figure 3.2).

[3.3] http://greenforecast.com/wp-content/uploads/2013/04/interconnected.png

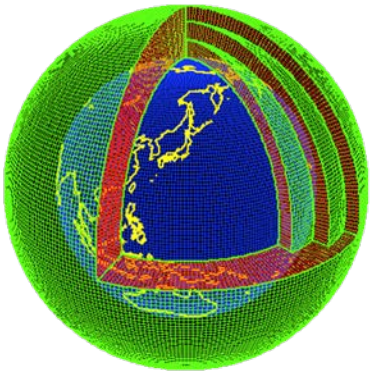

Figure 3.2: Schematic representation of a global 3D grid

Accurate initial and boundary conditions are crucial for accurate NWP simulations. The WRF model can use different analysis or reanalysis datasets for initialization. In this project, ERA-Interim, a third-generation reanalysis dataset was used (Dee et al. 2011).

3.1 WRF configuration

Most wind power plants under contract with HQD are located in the Gaspésie-Iles-de-la-Madeleine, Bas-Saint-Laurent and Chaudières-Appalaches regions as shown in Figure 3.3. Given that many wind plants are located in relatively complex terrain consisting of hills/mountains, forests and in close proximity to the St. Lawrence River, a final grid spacing of 3-km was selected for the WRF simulations in order to capture important wind patterns (e.g., channeling through mountain passes, katabatic winds, mountain waves, lake and sea breezes, low-level jets) and temperature gradients (temperature inversions, thermal stability, etc.), as well as to explicitly resolve clouds, which strongly influence icing conditions (freezing rain and rime ice). NWP models with grid spacing coarser than 4-5 km cannot explicitly resolve cumulus clouds, and may miss significant terrain features and other influences. A grid resolution much finer than 3-km, greatly increases computational demands. The 3-km grid spacing strikes a balance between computational time and the need to resolve localized terrain, roughness effects and clouds.

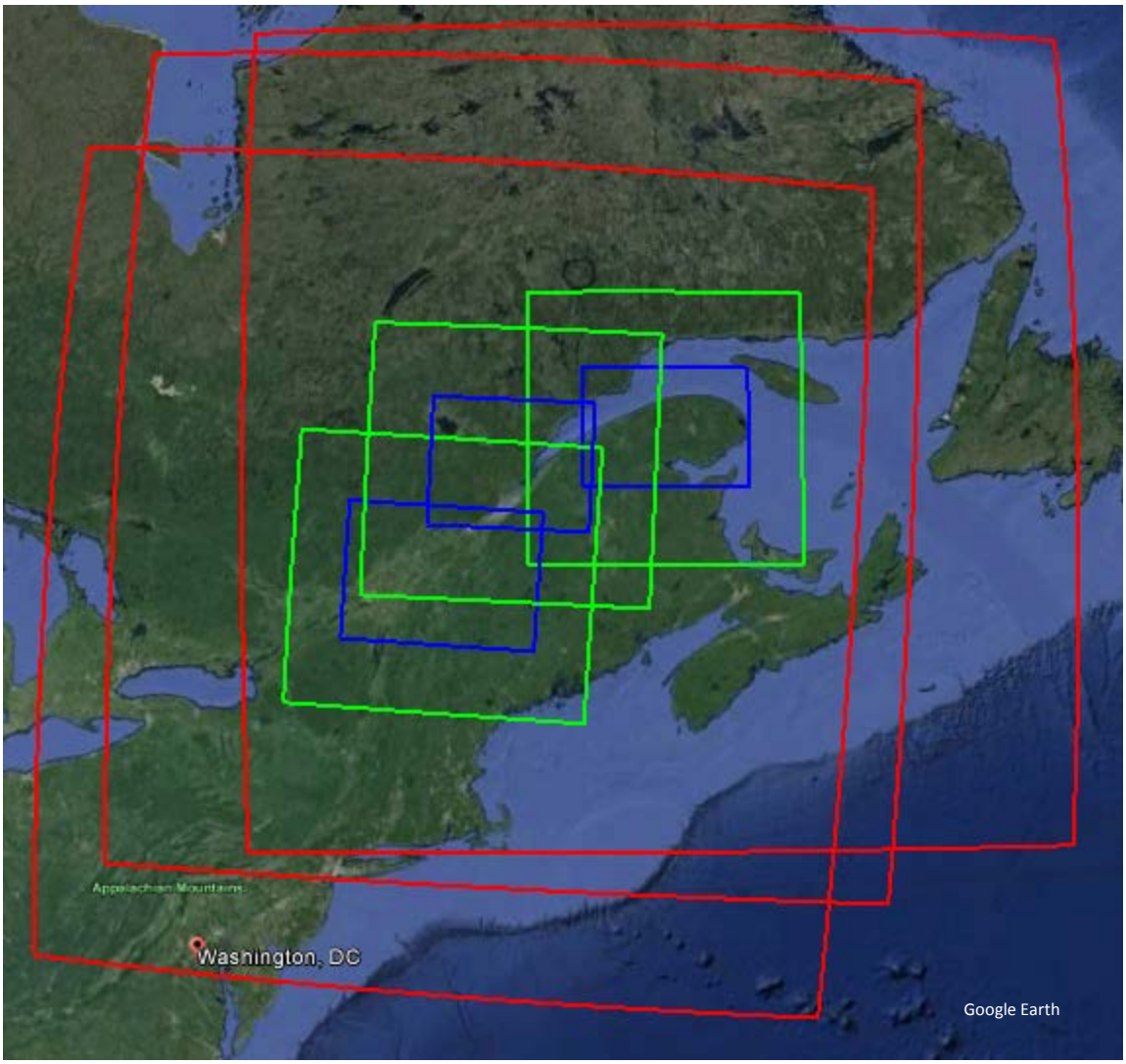

Figure 3.3: Location of the three 27-9-3 km WRF grids overlaid on the project area. The 3-km resolution grids (blue) are nested within 9-km (green) and 27-km (red) grids.

AWST relied on the WRF model for this project, which has undergone extensive testing and validation and been found to be numerically stable. WRF simulations were initialized by the ERA-Interim reanalysis dataset. The ERA-Interim reanalysis is produced by the European Center for Medium-Range Forecast (ECMWF) at a 0.75 degree resolution (~75 km) and includes the 1979-2015 project period. Studies by AWST and others (Brower et al. 2013, Lileo and Petrik 2011, Decker et al. 2012) show that the third generation reanalysis datasets have superior accuracy in term of their correlation to tall meteorological met mast data. Another critical aspect is their homogeneity over long time periods, to avoid introducing false trends or spurious discontinuities. Again, studies have shown that the ERA-Interim dataset is more homogeneous than other reanalysis datasets including CFSR, MERRA and NCEP/NCAR (Brower et al. 2013, Lileo and Petrik 2011, Decker et al. 2012). The ERA-Interim reanalysis data is available on a 6-hour time interval and served as initial and boundary conditions to the WRF simulation.

Dynamical downscaling is a method in atmospheric modeling which is designed to provide consistency across different parts of a domain while keeping computational demands manageable. WRF was set up to run three nested grids simultaneously with a horizontal grid spacing of 27, 9 and 3-km (see Figure 3.4). In essence, different scales of motion are resolved by grids with different resolutions. A ratio of 3 between the parent and child grid resolution (e.g. 27 vs. 9-km, 9 vs. 3-km) ensures a proper energy cascade from the large scales to the small scales, which is mainly due to the non-linear interactions. The first two grids, at 27-km and 9-km, respectively, resolve successively finer scales across the whole region. These grids pass the boundary conditions to the various innermost 3-km grids, each of which modifies the atmospheric circulations in response to a consistent set of surface forcings from the terrain elevation, land cover, soil temperature and moisture, etc. In other words, the data are passed from one grid to the next in a way that allows the model to develop the finest scales in a consistent way.

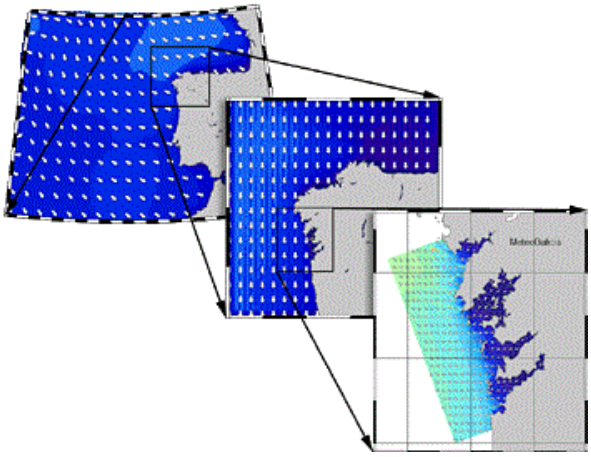

Figure 3.4: Dynamical downscaling based on nested grids representing the 27, 9 and 3-km resolution WRF simulations.

Continuous simulations were run in one-month blocks as indicated in Figure 3.5.For this project, an adequate buffer (~10 grid cells) between any site and the grid boundary was ensured, in order to maintain consistency in the time series generated by different grids. As mentioned in the paragraphs above, the spectral nudging and grid nesting will ensure consistency in the larger scale circulations. The surface forcing such as terrain elevation, land cover, soil temperature and moisture will drive the mesoscale circulations. The WRF model will respond in a similar fashion to the same surface forcing given that the physics options (radiation, cloud convection, cloud moisture, PBL turbulence, etc.) will remain the same for all WRF grids. Small-scale turbulence cannot be controlled. In any case, a 3-km resolution WRF simulation will resolve features of about 10-20 minutes in time scale.

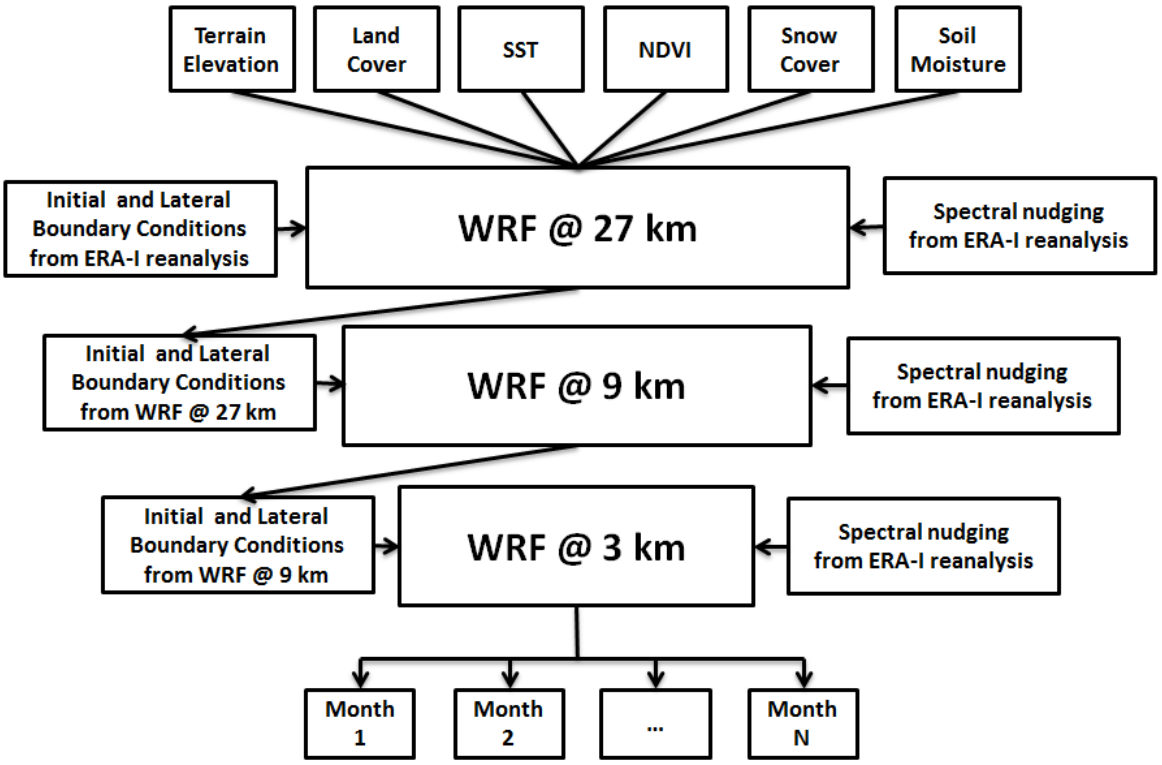

Figure 3.5: Diagram of the WRF modeling process. Consecutive 1-month long simulations were carried out to capture the local wind climate at each wind plant for the complete 1979-2015 period. SST and NDVI refer to sea surface temperature and normalized difference vegetation index, respectively.

3.2 WRF wind speed and temperature validation

The 3-km WRF simulations were evaluated against several pre-construction met masts provided by HQD. The met mast data were quality-controlled according to the procedure described in Section 2. Given that the observed meteorological fields at the tall towers typically consist of wind speed and direction at several heights and temperature, the validation of WRF was limited to wind speed, wind direction, turbulence intensity and temperature.

As a rule of thumb, NWP models tend to better predict the temperature field than wind speed or cloud cover due to random and coherent small scale turbulent fluctuations in the wind flow and that cumulus clouds cannot be fully resolved unless the grid resolution is very fine (on the order of 100 m).

AWST compared the modeled WRF meteorological time series against measurements from the met masts on an hourly time interval over the same concurrent period as the observations. WRF simulations at 3-km grid spacing are not equivalent to a point measurement such as a met mast. However, simulated WRF time series correlate quite well with observations in time and space at most sites, and most biases can be corrected by a simple scaling.

The validation was performed at the 23 pre-construction met masts detailed in Table 2.2. The results are summarized in Table 3.1. On average, the coefficient of determination (R^2) was 0.82 on a daily basis and 0.66 on an hourly basis. With one exception (M1), the values are relatively good (0.7 – 0.9 daily R^2) for wind energy application, using either surface or modeled weather data. The reasons for the relatively poor correlation at M1 are unknown, but may be related to the relatively poor data recovery at this tower (54%).

The mean wind speed biases (modeled - observed) shown in Table 3.1 average near 0.09 m/s across all met masts and range from -1.6 to 2.1 m/s on an hourly basis. Similar to the R^2, the biases are relatively good for model simulations. Note that the modeled wind speed bias is removed when the WRF simulations are adjusted to on-site measurements (see Section 3.3).

Table 3.1: Comparison of 3-km WRF time series against 23 pre-construction met masts

Site Name	Data Recovery (%)	Daily R^2 at Top Height	Hourly R^2 at Top Height	Mean Modeled Wind Speed at Top Height (m/s)	Mean Observed Wind Speed at Top Height (m/s)	Mean Wind Speed Bias at Top Height (m/s)
M1	54	0.59	0.48	10.06	8.02	2.05
M2	66	0.80	0.64	6.95	8.18	-1.23
M3	53	0.81	0.67	9.71	9.64	0.07
M4	63	0.78	0.62	6.94	6.85	0.09
M5	76	0.80	0.63	8.43	8.04	0.39
M6	56	0.84	0.67	6.77	8.24	-1.46
M7	52	0.82	0.64	6.01	7.39	-1.38
M8	91	0.86	0.65	7.18	6.67	0.51
M9	88	0.83	0.66	7.40	7.04	0.36
M10	74	0.88	0.70	8.11	7.90	0.21
M11	89	0.81	0.55	5.22	5.43	-0.21
M12	56	0.83	0.74	9.46	8.98	0.48
M13	51	0.71	0.62	9.36	7.77	1.60
M14	52	0.79	0.68	9.05	8.51	0.54
M15	46	0.86	0.70	6.94	6.20	0.75
M16	65	0.83	0.65	6.73	6.77	-0.05
M17	59	0.89	0.71	7.36	7.31	0.05
M18	38	0.90	0.73	8.04	9.61	-1.57
M19	57	0.87	0.70	7.57	6.52	1.06
M20	65	0.73	0.57	8.06	7.45	0.61
M21	75	0.86	0.67	7.04	7.32	-0.28
M22	70	0.82	0.67	7.50	7.21	0.28
M23	66	0.76	0.56	5.85	6.57	-0.73
Average	**63**	**0.82**	**0.65**	**7.64**	**7.55**	**0.09**

Next, AWST focused on two sites to look closely at the differences between the 3-km WRF simulations and the pre-construction met mast data. The M21 and M5 met masts were chosen as

typical examples of intra-hourly correlation and site characteristics, with reasonably good data recovery and measurement heights close to the model levels. The M21 and M5met masts are located in two different mountainous and forested areas, the former in the Bas-St-Laurent region and the latter in the Chaudière-Appalache region.

The scatterplots in Figure 3.6 and Figure 3.7 indicate that there's a fair amount of dispersion between the modeled and observed hourly wind speeds (right-hand plots). This is due to error in the magnitude and especially the timing, or phase, of small-scale fluctuations in speed. Phase errors can produce large errors in speed due to predicting storm or other weather systems arriving a little too soon or a little too late. Most of these timing errors are eliminated in the daily averages (left-hand plots), which show much less scatter and a higher R^2.

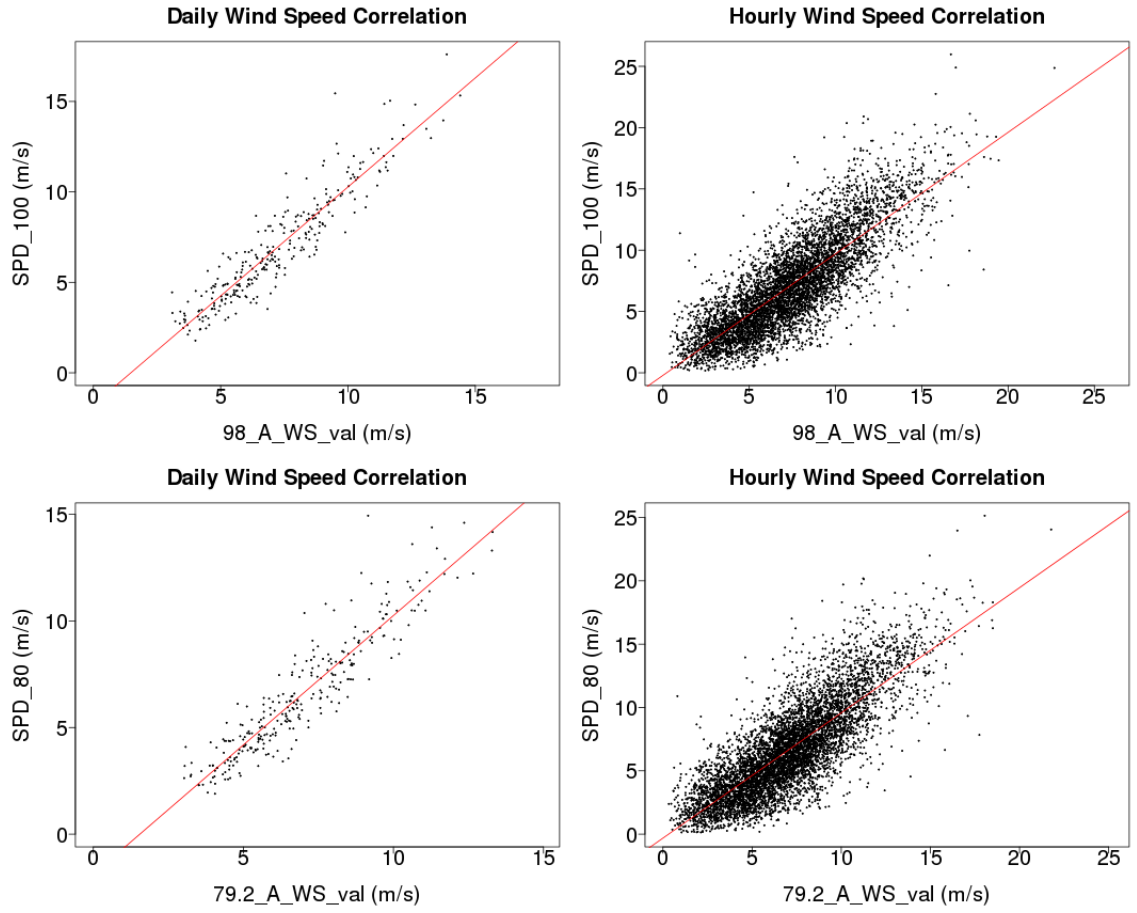

Figure 3.6: Scatterplots of daily (left panels) and hourly (right panels) wind speeds between the observed (X axis) and modeled WRF (Y axis) data at M21. The top panels show results for the highest anemometer height (~ 100 m) while the bottom panels correspond to an intermediate height (~ 80 m).

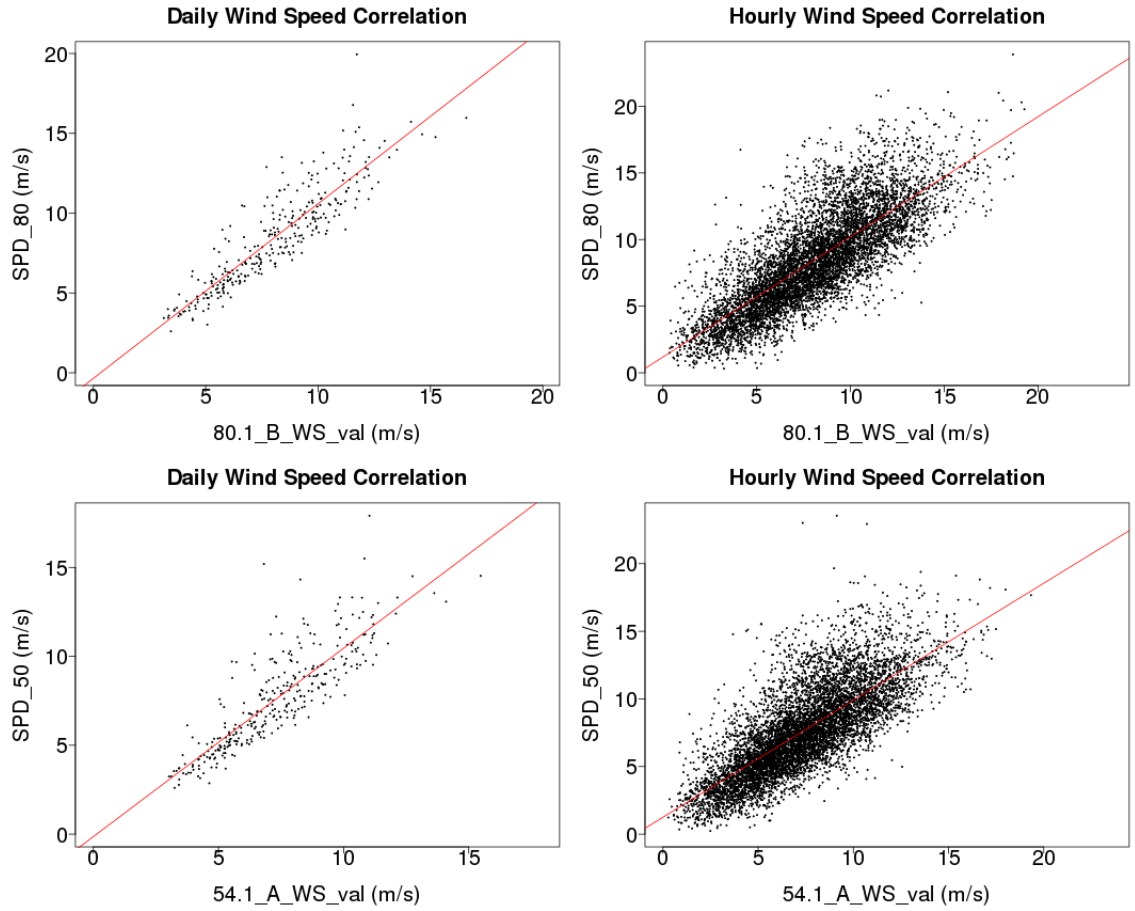

Figure 3.7: Scatterplots of daily (left panels) and hourly (right panels) wind speeds between the observed (X axis) and modeled WRF (Y axis) data at M5. The top panels show results for the highest anemometer height (~ 80 m) while the bottom panels correspond to an intermediate height (~ 50 m).

It is important for the NWP model to reproduce the observed wind direction distribution, as errors in the wind rose can lead to large errors in topographic effects and turbine-induced wake losses. The modeled and measured wind roses are in good agreement (see Figure 3.8 and Figure 3.9). The M5 site shows prevailing wind directions from the west sectors, which are typical of the large-scale circulations in Québec, largely influenced by the polar jet stream.

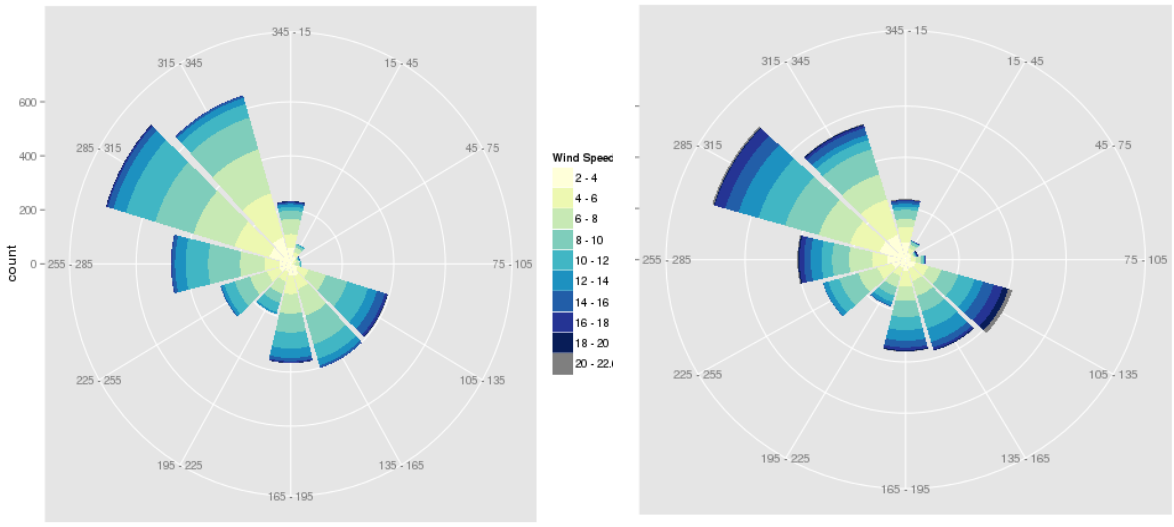

Figure 3.8: Modeled (left panel) and observed (right panel) wind rose at M21 at 100 m above ground

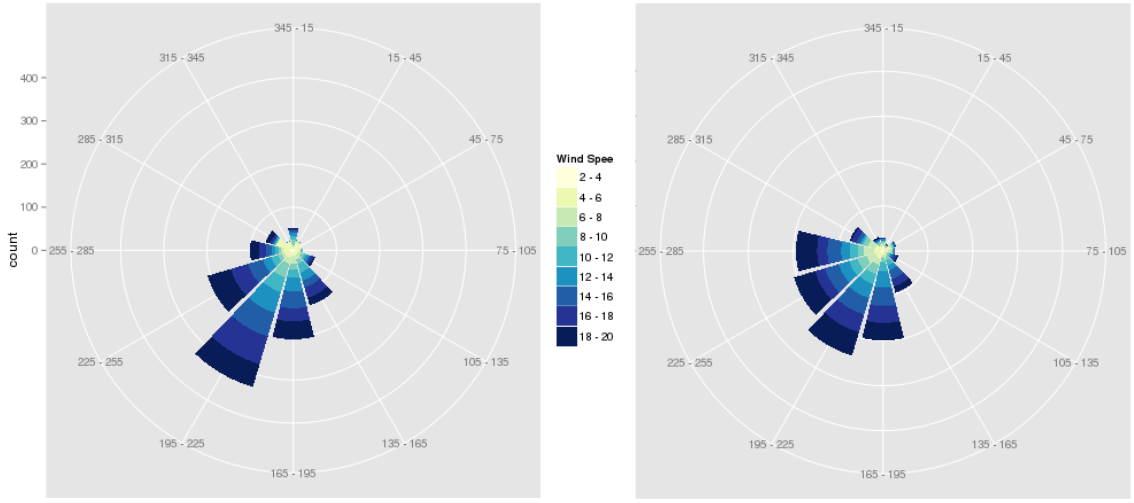

Figure 3.9: Modeled (left panel) and observed (right panel) wind rose at M5 at 65 m above ground

Seasonal and diurnal wind speed patterns are important to capture because variations in available wind power by time of year and time of day, as well as its correlation with the electrical loads, can impact the transmission network and non-wind generating sources (e.g. unit commitment, operating reserves, storage). In Quebec, large-scale pressure systems tend to become more

intense during the winter season, therefore winter wind speeds tend to be higher than summer speeds. In addition, the effect of daytime heating and nighttime cooling on the depth of the PBL usually causes wind speeds to be lower during the day than at night at hub height (~100 m) and the opposite near the surface (~10 m). Figure 3.10 and Figure 3.11 indicate that the WRF simulations replicate the seasonal and diurnal profiles with reasonable fidelity. Upon visual inspection of the monthly and diurnal profiles at every site, no systematic bias by time of year or time of day was evident, although some sites seem to have a larger wind speed bias during the winter season. In general, WRF agrees relatively well with the observed profiles.

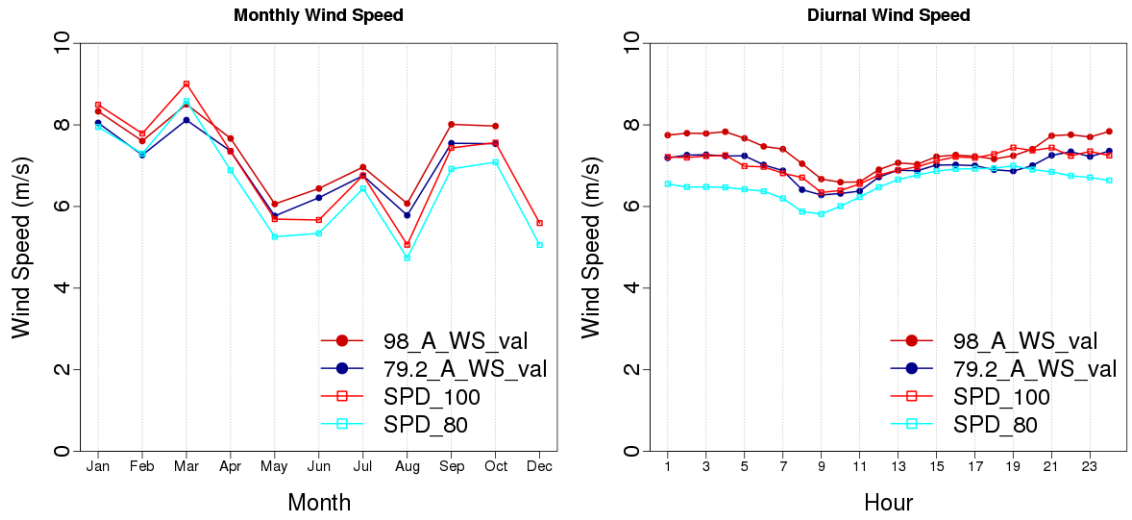

Figure 3.10: Average monthly (left panel) and diurnal (right panel) wind speed profiles at M21. The timestamps are in local standard time (LST).

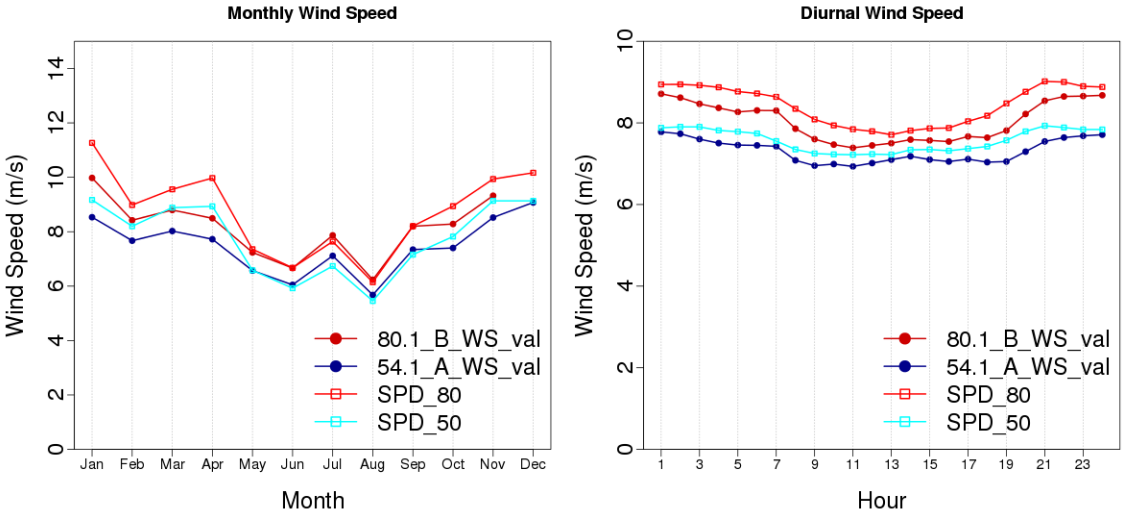

Figure 3.11: Average monthly (left panel) and diurnal (right panel) wind speed profiles at M5. The timestamps are in local standard time (LST).

After validating the WRF wind speeds, turbulence intensity (TI) was evaluated. While TI is a key input to determine the mechanical load a wind turbine can sustain (which is outside of the scope of this project), TI has an impact on the wind turbine power curve, as well as the propagation and decay of turbine-induced wakes. TI is a meteorological field that is typically not picked up as well as wind speeds by NWP models. Although the shape of the TI versus wind speed curve is correct with TI reaching an "asymptotic" value as the wind speed increases, the modeled TI curve is biased low (see Figure 3.12 and Figure 3.13). For instance, the average TI at wind speeds of 15 m/s, an IEC standard called "reference TI" (IEC 64100-1), is approximately 5 percentage points lower for WRF compared to the met mast measurements at M21 and M5. Discarding wind speeds below the cut-in of the turbine power curve, finds that the modeled TI values are systematically lower than the observed ones by 2-3 points at low to moderate wind speeds and about 5 points under high winds.

TI is derived from the turbulent kinetic energy (TKE) as shown in equation (1). TKE is one of the prognostic variables in the WRF model. The TKE budget equation describes physical processes that generate turbulence (Stull 1988). The conversion to TI as measured by a cup anemometer assumes the single vertical and two horizontal components of TKE are equal; this explains the 2/3 factor. Nonetheless, it is clear the modeled TI is biased low at most wind speeds.

$$TI = 2/3 * SQRT(2*TKE) / SPD \quad (1)$$

Taking into account the effective grid resolution of the WRF model (Skamarock 2004), the 3-km grid spacing WRF simulations will explicitly resolve atmospheric features on timescales of approximately 10 to 20 minutes. The PBL scheme that deals with the TKE budget equation, if it is functioning properly, gives a proper average value of features that vary on the order of seconds to a few minutes. Thus, some fluctuations on the 5-15 minute timescales may not be resolved by the NWP model. This could partly explain the discrepancy between the TI modeled by WRF versus measured by a cup anemometer on a met mast. Another factor that might be partly responsible is the assumption of equal horizontal and vertical components, which will break down for turbulent scales approaching or exceeding the height of the measurement. Nevertheless, the ambient TI modeled by WRF was found to have a negligible impact in the Openwind simulations when converting meteorological conditions (e.g. wind speeds) into wind power generation. This can be explained because two competing effects due to the lower WRF-derived TI are balancing each other to a certain degree: 1) the "knee" (or curvature) of the power curve near the rated wind speed is smoothed and wider and 2) the velocity deficit in the wake region recovers more slowly. The first effect will typically increase the amount wind power generated while the second will decrease it.

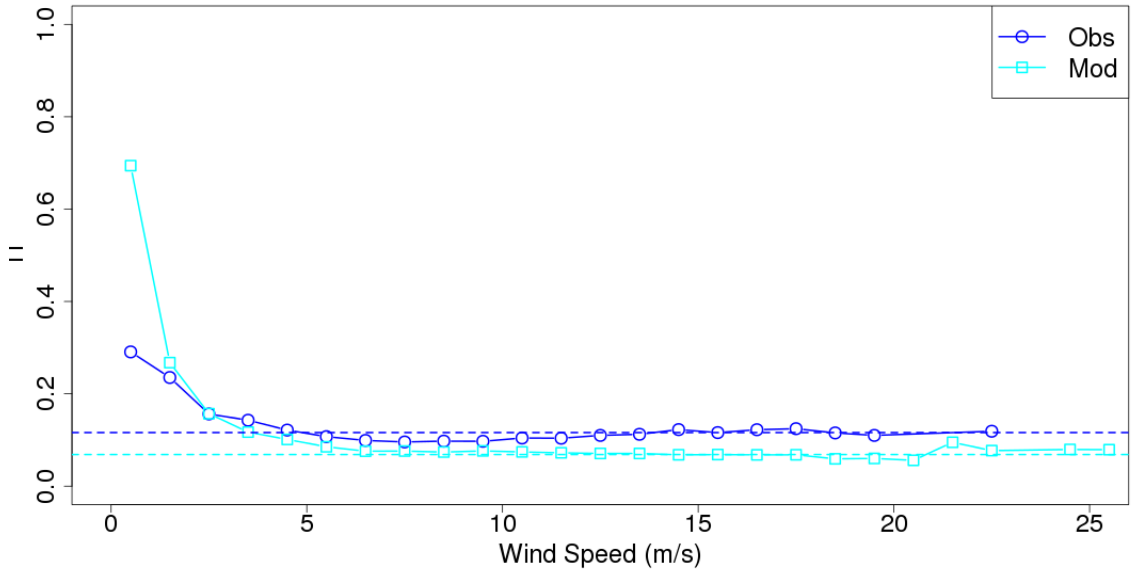

Figure 3.12: Turbulence intensity at the M21 met mast for the modeled (cyan) and observed (blue) datasets. The dashed lines correspond to the reference turbulence intensity.

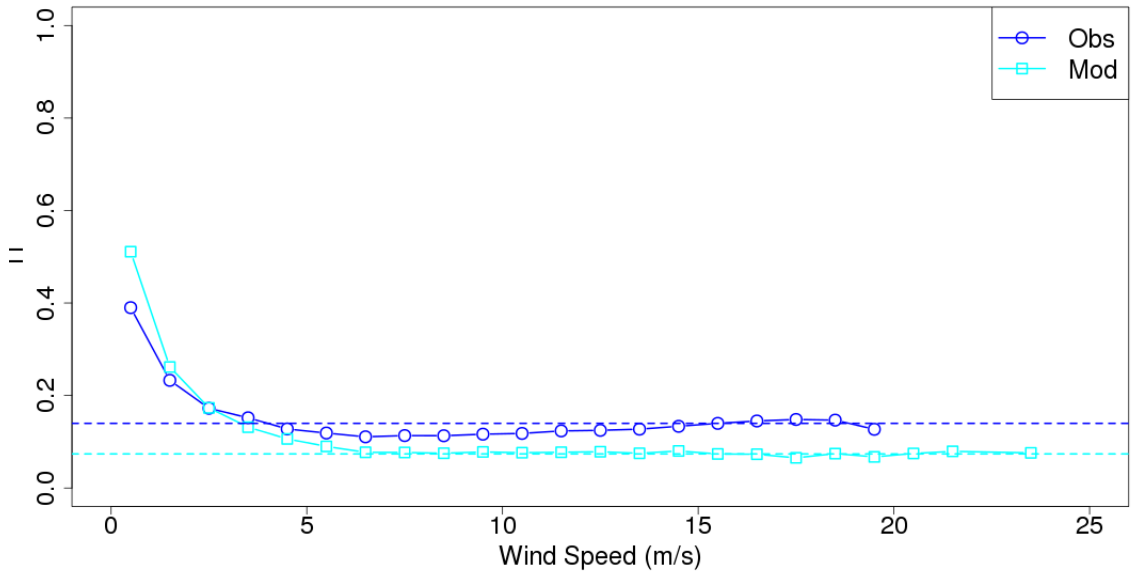

Figure 3.13: Turbulence intensity at the M5 met mast for the modeled (cyan) and observed (blue) datasets. The dashed lines correspond to the reference turbulence intensity.

In general, NWP models have better skill at predicting temperatures than wind speeds. The temperature correlations between the WRF model outputs and the onsite measurements are

high, with an R^2 averaging 0.95 across all met masts. The scatterplots in Figure 3.14 and Figure 3.15 illustrate correlations of 0.98 and 0.96 at M21 and M5, respectively.

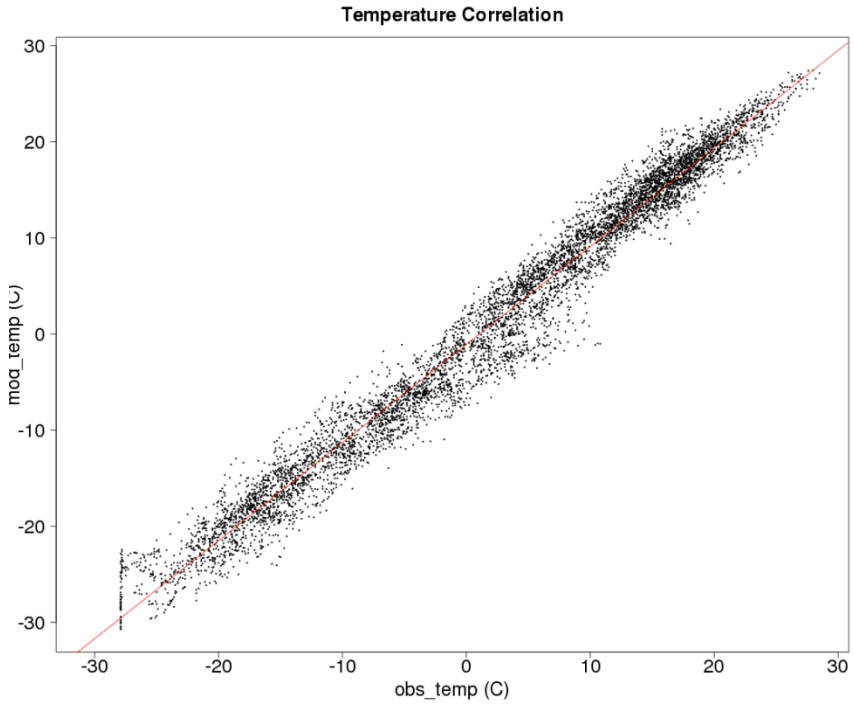

Figure 3.14: Scatterplots of temperatures between the observed (X axis) and 3-km WRF (Y axis) data at M21. The coefficient of determination (R^2) is 0.98.

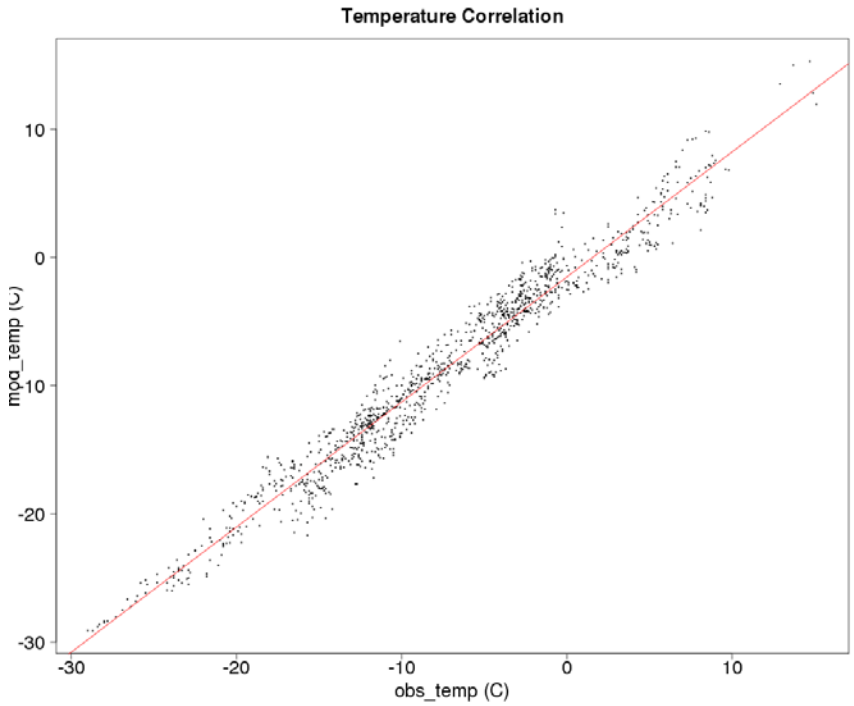

Figure 3.15: Scatterplots of temperatures between the observed (X axis) and 3-km WRF (Y axis) data at M5. The coefficient of determination (R^2) is 0.96.

Although it may be hard to detect in the temperature scatterplots in Figure 3.14 and Figure 3.15, the WRF model outputs are biased low compared to onsite measurements. It is a known bias in WRF that originates from the Noah land surface model (Garcia-Diez et al. 2013). AWST's validation indicates that WRF temperatures tend to be too cold, with a bias of -2.3 C. This low temperature bias is consistent between seasons and is similar to an average temperature bias of -1.75 C found in a previous study carried out by AWST across multiple meteorological stations in the US and Europe.[3.4]

A temperature bias near the surface in the WRF model can and probably does change the structure of the PBL which in turn modifies the wind speed profiles. Garcia-Diez et al. (2013) carried out sensitivity studies using three different PBL schemes within WRF but none solved the low temperature bias. This study was replicated using the Mellor-Yamada-Janjic (MYJ) and Yonsei University (YSU) PBL schemes with similar results.

The WRF temperature bias will have an impact on the temperature shutdown losses as the temperature will fall below the cut-out temperature more often in the simulations than in reality. However, the impact is small. The temperature distributions at M21 and M5 are shown in Figure 3.16 and Figure 3.17, respectively. The temperatures rarely reach below -30 C in the winter or above 30 C in the summer at any sites. Across all sites, the frequency of occurrence of temperatures below -30 C in the WRF simulations is 0.3% on average, whereas the observed

[3.4] WRF simulations at 27-km grid spacing were validated against 15 met stations in the US and 13 met stations in Europe. In both regions, the mean temperature bias was -1.75 C.

frequency is 0.2%. The difference, 0.1%, has a negligible impact on energy production. The highest frequency of temperatures below -30 C is at the P24 wind farm which nears 0.9%. Temperatures never exceed the high-temperature shut-down, so this loss is unaffected. The icing loss model built in Openwind (see Section 4) should not be impacted by the WRF temperature bias, since it is based on a generalized additive model (GAM) where the relative temperature values matter, not their absolute values.

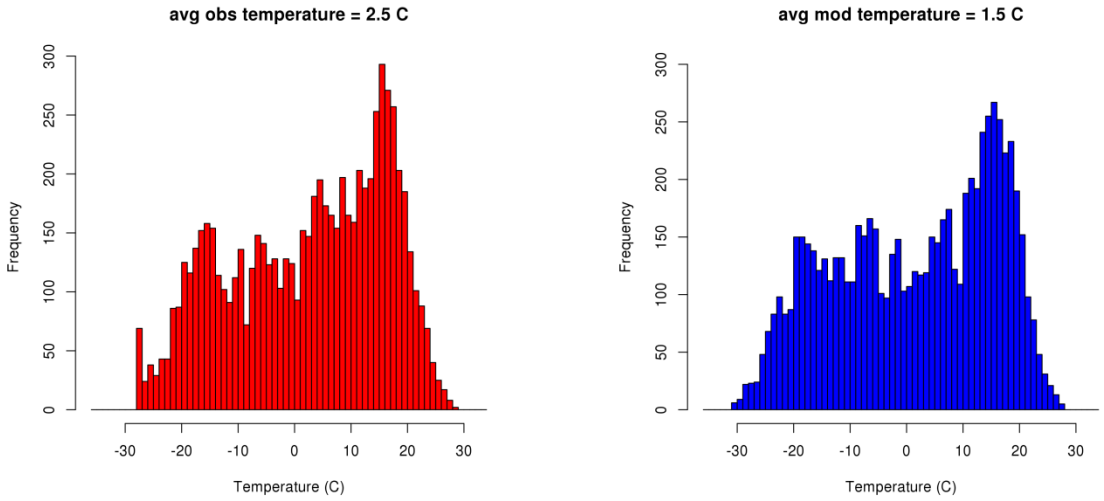

Figure 3.16: Observed (left panel) and modeled (right panel) temperature distribution at M21 at 90 m above ground

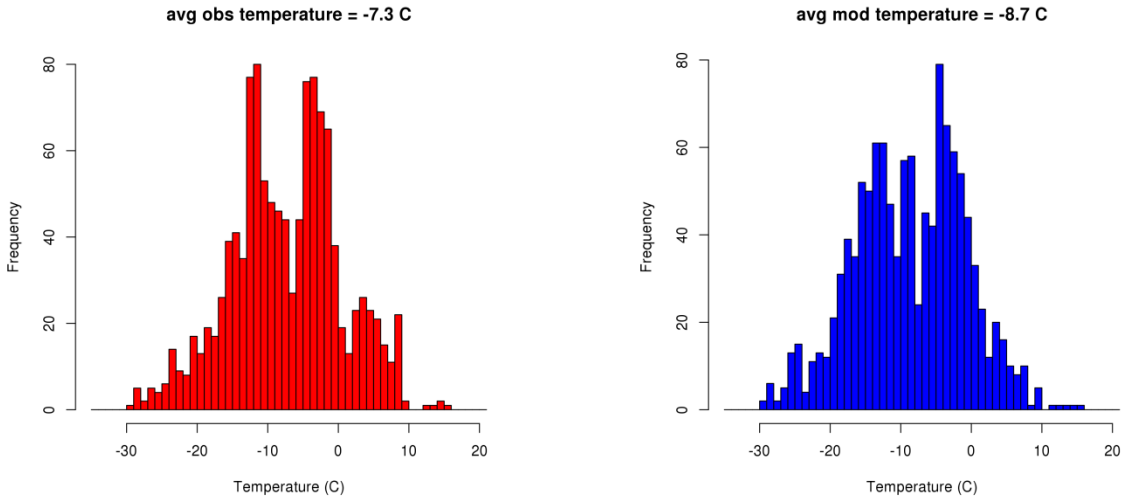

Figure 3.17: Observed (left panel) and modeled (right panel) temperature distribution at M5 at 4 m above ground

3.3 Scaling the WRF time series

The preceding section demonstrated that the WRF meteorological time series achieve a reasonably high degree of correlation to the onsite measurements, specifically regarding wind speeds, directional distributions, and temperatures. It suggests that the 3-km grid resolution model can capture most of the relevant synoptic and mesoscale circulations, which determine the variations in wind plant production over time.

Before converting the WRF data to wind plant production, however, it is necessary first to correct for biases to ensure that the average wind resource available for conversion to power is correct. This was done by scaling the WRF wind data to match our best estimate of the average wind speed at each site. AWST took two different scaling approaches depending on whether the wind plant was operational for at least 9 months or not:

- For non-operational wind plants, wind speeds were extracted from the WRF simulations and interpolated to the height and location of each preconstruction met mast. The wind speeds were then scaled by a multiplicative factor so that the average modeled speed matched that of the onsite met mast measurements for concurrent valid records.
- For the operational wind farms, rather than scale the WRF speeds to match preconstruction measurements, we scaled them so that the net power production from the Openwind model matched the observed net power production at each plant.

Independently of the speeds, the modeled temperature profiles were adjusted to account for the differences between the 3-km elevation in WRF and the 200-m elevation from the global digital elevation model (DEM) map. The global DEM map is based on the Shuttle Radar Topography Mission (SRTM) dataset. The temperature adjustment assumes a standard temperature lapse rate of -6.5°C/km. Note that the WRF temperature field was not adjusted with the on-site measurements at the met masts. The atmospheric pressure was also adjusted by using the hypsometric equation with the adjusted WRF temperatures. Once the WRF temperature and pressure fields were adjusted, the air density and the relative humidity were corrected accordingly. These parameters were used as inputs to the Openwind simulations.

3.4 WRF coupled to a microscale model

The accurate prediction of a wind farm's energy production is dependent upon an accurate and detailed understanding of the spatial distribution of the wind resource across the project area. Towards the end of the 1990s, DTU Wind Energy and AWS Truepower independently pioneered a method to couple a mesoscale and microscale model for wind resource characterization at spatial resolutions on the order of 10-100 m, respectively the KAMM/WAsP (Frank and Landbergh 2001) and SiteWind (Brower 1999, Beaucage et al. 2014) approaches. In AWST's approach, known as SiteWind, a NWP model is run using nested grids up to the meso-gamma scales (~1 km). Then, the mean wind flow modeled by the mesoscale model is downscaled to a 50-m grid spacing using a diagnostic mass-conserving model. Recently, a few studies (Poulos and Kumar 2013, Beaucage et

al. 2014) have shown that on the whole NWP-based models generally performed better than other models, although no single model performed best at all sites.

For this project, WRF was run with nested grids to reach a 3-km resolution grid as described in Section 3.1. Then, the wind climate statistics were computed and binned by wind direction. These wind climate statistics provided the wind data inputs to the microscale model, WindMap, as shown in Figure 3.18. The mass-consistent model downscaled the mean wind flow to a final resolution of 50 m.

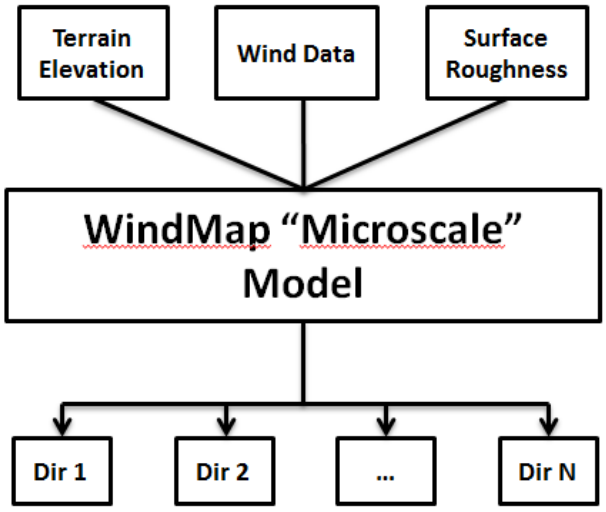

Figure 3.18: Diagram of the WindMap microscale modeling process.

In order to properly capture the surface forcings at the site, the WindMap model ingests high-resolution terrain and land cover maps. The terrain elevation map is obtained from the Shuttle Radar Topography Mission (SRTM) with a 1 arc-second grid spacing (~ 30 m) while the land cover map consists of the GeoBase LCC2000V data from the Government of Canada. In order to run the microscale model efficiently and keep file storage manageable, the WindMap simulations were divided into 6 different domains covering all 39 wind farms as shown in Figure 3.19.

The WindMap model outputs are stored in binary wind resource grid (WRG) files, which are later used by the Openwind software to extrapolate the adjusted WRF meteorological time series to the turbine sites and estimate wind power generation.

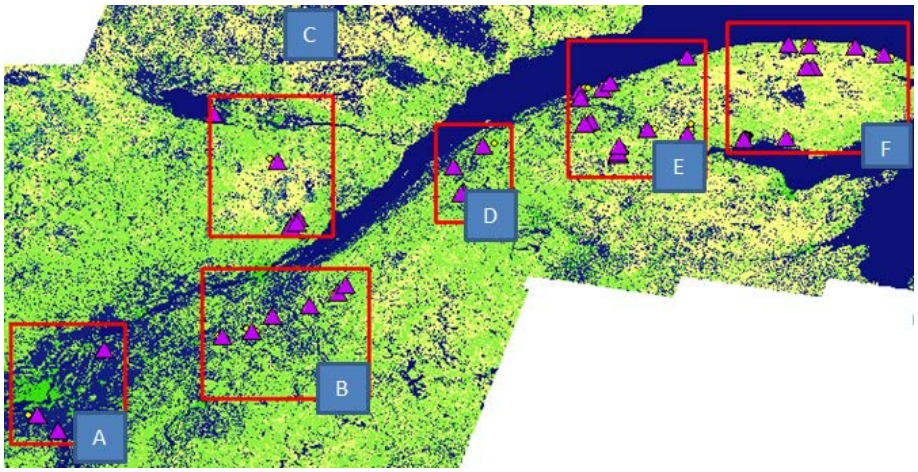

Figure 3.19: Land cover map of the Southern Québec province and six WindMap domains.

4. MODELED WIND POWER GENERATION TIME SERIES

The primary objective of this project was to create realistic long-term wind power time series that mimic the operational behavior of the 39 existing and planned wind plants to support HQD's analyses of the contribution of wind power plants to the power system. As discussed in Section 3, long-term meteorological time series were created by the WRF model and adjusted to match our best estimate of site conditions. In this section, how these adjusted data were converted into wind power generation with the Openwind software is discusssed.

The first step to converting the modeled met data into wind power generation is to compute the gross power generation, or the theoretical amount of power a wind turbine or a wind farm would produce assuming no wind plant losses. The next step consists of estimating energy losses in each of several categories. The losses are tracked separately.

The net energy production is derived by subtracting all the wind plant losses from the gross energy. The net power represents the total power at the electrical connection point of the wind farm to the grid, typically a substation.

The losses at any wind plant are classified in the following categories:

- Wake effects:
  - Internal wake effects (inside the project)
  - Wind farm shadowing (wake effects from neighboring wind farms)
- Availability:
  - Scheduled maintenance
  - Outages (substation and utility grid, plant restart after grid outage, force majeure)
- Environmental:
  - Icing
  - Low temperature shutdowns
  - High temperature shutdowns
  - High Wind Hysteresis
  - Blade degradation
- Electrical:
  - Electrical efficiency (transformers, electrical collection system, etc.)
  - Power consumption of wind turbines (lighting, O&M facility, cold weather package, de-icing system, etc.)
- Turbine performance:
  - Sub-optimal operation (yaw and blade pitch misalignments, control anemometer calibration, etc.)
  - Power curve adjustment (expected turbine performance relative to advertised power curve)
- Curtailments:
  - Directional curtailments (for turbines spaced less than 3 rotor diameter distance from each other)
  - Environmental curtailments (habitat concerns, noise constraints, shadow flicker, etc.)
  - Grid-related or power purchase agreement curtailments

AWST estimated gross and net energy production as well as losses for the following categories: wakes, availability, environmental (low and high temperature shutdowns, high wind hysteresis, icing), turbine performance and electrical losses (electrical efficiency and turbine power consumption). Two losses mentioned above were not included in the scope of this project: curtailment and blade degradation. HQD confirmed that there were no curtailments applied to the wind plants. In addition, the blade degradation loss is marginal and difficult to estimate accurately due to nacelle-mounted anemometer calibration issues.[4.5] For this reason, these two losses were removed from the study. The following sections describe the SCADA analysis on which several losses were based, the Openwind setup and configuration, and the methods used to simulate energy losses conforming to the observed plant behavior.

4.1 SCADA Analysis

The first step in the process was to analyze the SCADA data from operational wind farms to derive the actual losses experienced by the wind projects. These observed losses were then used to verify and, where necessary, tune the Openwind model parameters to reproduce the observed plant behavior with sufficient fidelity to satisfy HQD's objectives. Note that the use of SCADA data for this purpose was possible only for certain loss categories (albeit very important ones), in particular availability, environmental losses and electrical. Wake losses could not be estimated from the data and were based entirely on the Openwind model. Other losses, such as turbine performance, were calculated following AWST's standard approach in pre-construction energy studies.

To derive the actual availability, environmental and electrical losses from the SCADA data, the data were analyzed to estimate the potential power generation at all times as if the turbines were performing as well as they normally can. The difference between this potential energy (sometimes called possible energy) and the energy actually produced at any given time is the lost energy at that time. The IEC 61400-26-2, Annex A, offers several methods to estimate the potential power generation. AWST's method aligns with Method A, in which the nacelle-anemometer wind speeds and concurrent power generation from the SCADA system are combined to establish a potential power curve for each turbine.

Lost power was calculated from the difference between the actual and potential power generation. In a subsequent step, AWST calculated the lost energy by turbine state, e.g. icing, low temperature shutdown, high-wind shutdown, and others, including unknown sources of downtime. Known and unknown sources of downtime were then summed to estimate the total plant availability at each time step for each plant. These time series of observed plant availability were then aggregated across all sites, and from this aggregate time series a Markov transition matrix was calculated for input into the Openwind model, as described in Section 4.2.

[4.5] Typically, the energy losses due to blade degradation are on the order of 0.01% to 0.1% annually. These values are small in comparison to wake, availability and icing losses each of which averages around 4% to 8% annually in Québec.

A key challenge was to isolate the icing loss from other losses. AWST's method to derive icing losses from the operational SCADA data roughly follows the guidelines of the IEA Task 19. In our approach, the total lost energy due to icing is the sum of (a) the lost energy under an explicit turbine icing status codeand (b) the lost energy not specifically identified as icing-related but likely caused by icing based on meteorological conditions. For turbines with a blade heating system, there is the additional complication that the lost power under icing conditions could be a result of the blade heating power consumption rather than (or in addition to) icing effects.

An example of estimated lost energy is shown in Figure 4.1 for a period of 5 days in December 2013 at the P37 wind farm. The top line represents the potential energy production of the wind farm based on the potential historical power curve. The bottom line represents actual energy production from the SCADA system. The gap in between the two lines corresponds to the energy loss (excluding wake effects and electrical losses). The red bands indicate lost energy due to explicit icing states. The off-white band corresponds to lost energy due to identifiable effects not related to icing, such as low-temperature shut downs. Finally, the pink bands indicate lost energy due to unidentified sources, which considering the weather conditions is ascribed to icing.

The method used to estimate possible icing losses is not fool proof. Some periods ascribed to non-icing-related effects may in fact be icing, and vice-versa. Nevertheless, we believe the outcome of this analysis was the best possible dataset for developing the Openwind icing model for the plants in this study.

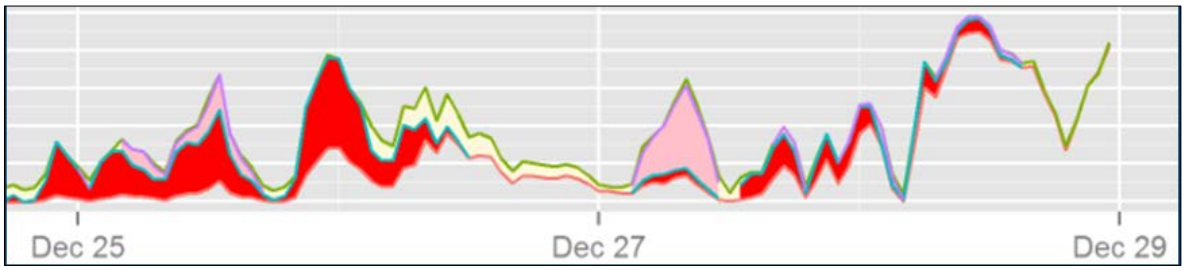

Figure 4.1: Lost energy due at the P37 wind farm between December 25-28, 2013.

4.2 Openwind Configuration

The Openwind software handled the conversion of the hourly WRF meteorological time series into wind power generation. Openwind is a wind resource assessment and layout optimization software developed by AWST. Several modifications were made to Openwind to turn each wind farm into a fully dynamic system by allowing the wind plant losses to vary from one time step to another. These new features are part of the available time-series energy-capture module.

Several inputs were used in order to run a time-series energy capture in Openwind:

- High-resolution terrain elevation map
- High-resolution surface roughness map
- Hourly WRF meteorological time series

- Binary WRG files from SiteWind
- Wind farm layout
- Turbine characteristic information

The high-resolution terrain elevation and surface roughness maps are the same as the ones used for the SiteWind simulations described in Section 3. Section 3 also details the process to create the hourly WRF meteorological time series as well as the 50-m resolution wind maps (i.e. binary WRG files) when coupling the WRF model outputs with the microscale model WindMap.

The wind farm layouts and turbine characteristic information were provided by HQD. The turbine characteristic files include such information as the hub height and rotor diameter, power and thrust curves, storm control settings, cut-in, cut-out and cut-back-in wind speeds, low and high temperature shutdown, temperature de-rating specifications, and de-icing systems. A total of 12 different wind turbine models made by five original equipment manufacturers (OEMs) were handled for this project.

Figure 4.2 provides an example of the Openwind interface for a project ready for an energy capture simulation. AWST selected between 1 and 4 WRF meteorological time series, each representing a separate virtual mast per wind farm. Although the WRF time series can capture most synoptic and mesoscale atmospheric features, high-resolution modeling is necessary to estimate the energy production of each turbine. This modeling was done in two steps: (a) extrapolation of wind speeds based on directional speed-up factors derived from the binary WRG files, and (b) a temperature adjustment based on terrain elevation.

Once the 50-m resolution binary WRG files are imported into Openwind, it calculates the speed-up ratios by direction sector between the mast location and each turbine. These speed ratios effectively account for the spatial variations in terrain elevation and surface roughness.

Openwind adjusts several WRF variables for each wind turbine location by considering the terrain elevation difference between the mast location and the turbine and then applying some standard corrections to temperature, atmospheric pressure, air density and relative humidity. This process allows for the weather conditions to vary among the turbines, with turbines at higher elevations typically experiencing lower temperatures, lower air density, and greater icing than turbines at lower elevations.

The Openwind energy capture tool runs the meteorological time series through the respective power curve at each turbine to estimate gross wind power generation adjusting for the effects of turbulence intensity and air density on the power curve. The remainder of this section describes the calculation in Openwind of the various losses to estimate net power.

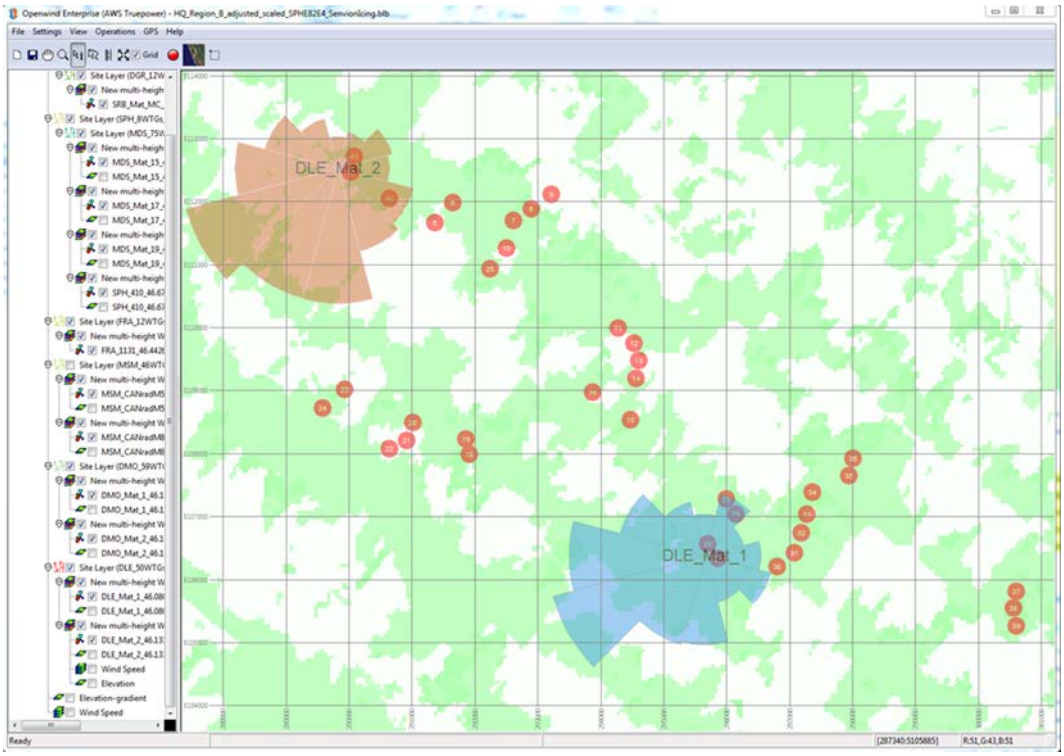

Figure 4.2: Example of an Openwind workbook with multiple layers including the surface roughness map (background colors), the wind turbine layout (red dots) and two masts (wind roses).

4.3 Methods for Simulating Wind Plant Losses

4.3.1 Wake Effects

When operating, wind turbines extract kinetic energy from the airflow, leaving the air downstream, i.e. the wake, with reduced speed and static pressure as well as greater turbulence (Crespo et al. 1999, Vermeer et al. 2003). This phenomenon is the source of significant energy production losses in wind power plants. In projects involving more than a handful of wind turbines, wake effects typically reduce power production by anywhere from 3% to 15% on an annual average. Furthermore, wake-induced turbulence can cause wear on the components of turbines, and for this reason, turbines are usually spaced no closer than three rotor diameters, and they may have to be shut down under certain conditions to satisfy the manufacturer's warranty.

AWS Truepower uses the Deep Array Wake Model (DAWM) inside Openwind to calculate wake losses (Brower and Robinson 2009). The DAWM actually contains two wake models. The first is the Eddy Viscosity model, which is based on the thin-shear-layer approximation of the Navier-Stokes equations assuming axisymmetric wakes of Gaussian cross-sectional form, as originally postulated by Ainslie (1988). The model equations ensure that momentum and mass conservation are observed simultaneously. As inputs, the wake model requires the ambient turbulence intensity at hub height, which influences the initial wake deficit behind each turbine and the rate of wake

dissipation; the speed and direction frequency distribution, based on a wind resource grid and associated WRF meteorological time series files; the locations of the turbines; and the turbine thrust coefficient curves. Validation of the Openwind Eddy Viscosity model is available online (AWS Truepower 2010).

In response to evidence that conventional wake models like the Eddy Viscosity model underestimate wake losses in deep (multi-row) arrays of wind turbines, especially offshore (Brower and Robinson 2009, Schlez and Neubert 2009), AWS Truepower implemented a second model designed to handle such situations. This model is loosely based on a theory developed by Frandsen (2007), who postulated that the effect of a deep array of wind turbines on the atmosphere could be represented as a region of increased surface drag, represented by a surface roughness length. Where the wind first impinges on the array, an internal boundary layer (IBL) is created, within which the wind profile is determined by the array roughness rather than by the ambient roughness. This IBL grows with downwind distance, and once its height exceeds the turbine hub height, the hub-height speed impinging upon turbines farther downwind is progressively reduced. According to the Frandsen theory, the effective array roughness is in the range of 1 m to 3 m, or typical of a forest, for mid-range speeds and typical turbine spacings.

In combining the two models, the DAWM implicitly defines “shallow” and “deep” zones within a turbine array. In the shallow zone, the direct wake effects of individual turbines dominate, and the unmodified Eddy Viscosity (EV) model is used to calculate wake deficits; in the deep zone, the deep-array effect is more prominent, and thus, the roughness model is employed. The DAWM has been validated at several offshore and onshore projects (Brower and Robinson 2012).

In addition to wake effects from turbines within the same wind farm, i.e. internal wakes, the turbine-induced wakes from a neighboring wind farm located upstream can impact the energy production. As a general rule inter-plant wake losses are assumed to be negligible for plant spacings greater than about 50 rotor diameters (about 5 km). This is especially true in the complex terrain and forested land cover typical of Quebec, which disrupt wakes through increased ambient turbulence due to the surface drag. Inter-plant wake losses are unlikely to be significant since only a few wind plants are located within 5 km of each other. Nevertheless, to the extent they occur, Openwind takes them into account since the simulation domains cover multiple projects at a time (see Section 3.4).

4.3.2 Availability

Availability losses occur when some turbines in a project, or the entire project, are unavailable for some reason but could otherwise be generating power. This can occur due to turbine faults or a failure of one or more turbine components.[4.6] It can also be caused by a failure or shutdown of the power grid or substation. Plant start-up problems, repair delays, fleet-wide turbine issues requiring retrofits, and other issues can cause extended periods of downtime that reduce the long-term average availability.

[4.6] Status codes that result in the turbine being shutdown.

Some observers have found a tendency for turbines to trip off under high wind conditions, which increases the energy loss (e.g. 3% down time may actually correspond to a 5% energy loss). An average availability loss of 2-10% is typically encountered in operation (Brower et al. 2012). Note that availability is defined in various ways. Contractual or turbine availability is often the figure quoted by plant operators. It is usually time-based, and follows definitions of the operators under their performance contracts. It tends to be lower than total plant availability, which includes downtime due to environmental or other conditions excluded from the contract, as well as outages of the plant systems and of the grid. In addition, being usually time- rather than energy-based, contractual availability can understate the energy loss.

AWST modeled time-varying wind plant availability within the Openwind software based on a Markov chain method. The Markov chain sets a random process in motion to simulate the transition from one plant state to another. The availability model simulates the change in number of turbines that are available, and therefore the change in availability loss, from one time step to the next. The main component of the Markov chain is a transition matrix, which indicates the probability of transitioning from any given current state any other state in the next time step. The matrix of transition probabilities was constructed for this project using operational HQD wind farm data, and thus the outcome reflects actual plant behavior. Within Openwind, for a given availability state, specific turbines are selected at random to be switched off. This allows the effect of availability on wake losses, for example, to be correctly modeled. From one time step to the next, only the minimum number of turbines that need to be switched on or off to arrive at the next availability state are selected in order to model the persistence of turbine downtime patterns.

HQD provided detailed maintenance schedules for each OEM. According to contracts with wind farm owners, planned maintenance is prohibited in the winter. Therefore, AWST developed two separate transition matrices - one for the winter season covering the period from December 1st through March 31st when routine maintenance is not allowed, and a second for the remainder of the year, i.e. April 1st through November 30th. As noted earlier, the transition matrices in the Openwind availability model were built using SCADA data from the 18 operational wind projects. Therefore, the availability model based on these transition matrices includes all the events that were recorded by the SCADA datasets. If there were force majeure events within that time period recorded in the SCADA system, then they will be represented in the transition matrices.

Some filtering of the SCADA data was necessary. Since the first year of operation typically entails significantly higher losses than subsequent years, the SCADA data was filtered to discard the first few months of operation rather than using the commissioning operation date of each plant. HQD analyzed each plant to estimate the shakedown period when most of the plant start-up problems were resolved and the necessary tuning and testing completed. Overall, it was estimated that the shakedown period lasted approximately 4 months at most wind farms.

Lastly, a turbine was considered available based on its status codes as reported in the SCADA data. There are between roughly 50 to 1000 status codes depending on the OEM. Only a handful of status codes are actually related to turbine availability. Turbines are considered “available” even

when an icing status code is reported in order to avoid double-counting when summing all the plant losses, i.e. availability and icing losses are separate.

4.3.3 Environmental - icing

Ice accumulation on a blade can disturb the smooth airflow causing a loss of lift which in turn causes a loss in energy production. In addition to reducing aerodynamic efficiency and thereby impacting the power generation of a wind turbine, icing on the blades can increase the mechanical load and fatigue as well as causing safety concerns if ice sheets are thrown off the blades. Québec's harsh winters mean that energy losses due to icing are one of the leading causes of lost production at many wind projects.

There are two main types of icing mechanisms: (a) in-cloud icing (which forms rime ice) and (b) precipitation icing (which forms glaze ice). The proportion of rime icing over precipitation icing varies across the Québec province based on the local climate and topography (Savadjiev and Farzaneh 2001, Yang et al. 2015), but the most severe icing effects come from ice storms, i.e. precipitation icing (Bendel and Paton 1981). Nevertheless, severe in-cloud icing can occur above the condensation level and the freezing level on freely exposed heights. On the leeward side of the mountains the descent of an air mass from higher to lower altitude results in internal heating of the air and evaporation of water droplets, diminishing icing risk. A local shelter of hills not more than 50 m higher on the windward side may give a significant reduction in ice loadings (IEC 60826).

Freezing rain and wet snow are the most common forms of precipitation icing, which result in a clear, solid glaze ice. Freezing rain occurs mostly on wide plains or basins where relatively deep layers of cold air accumulate during spells of cold weather (IEC 60826).

To create a wind power time series including icing losses, the onset and duration of icing conditions must be well represented by the modeling system. The timing of icing events should be captured at least partially by the WRF model. Predicting the ice accretion rate on the surface of the blades is more challenging, as it is a function of the icing type, blade characteristics, e.g. shape, size and composition, as well as atmospheric conditions, e.g. temperature, relative humidity and precipitation. Each type of ice has a different density, liquid water content, and adhesion properties, as shown in Table 4.1. Although the ISO 12494, Annex C, offers some guidance on a theoretical formulation for ice accretion rate, it is limited to cylinder such as a transmission wire, not the shape of a blade, and several efficiency factors, i.e. collision, sticking and accretion, must be estimated. A complicating factor is that the rotor blades rotate when there's enough wind for the turbine to generate electricity.

Table 4.1: Physical and meteorological properties related to atmospheric ice[4.7]

Type of ice	Density (kg/m^3)	Adhesion	Droplet size	Liquid water content	Air Temperature (C)	Mean Wind Speed (m/s)	Typical Storm Duration
Glaze ice	700-900	Strong	Large	Medium	-10 < T < 0	Any	Hours
Wet snow	400-700	Medium	Flakes	Very high	0 < T < 3	Any	Hours
Hard rime	700-900	Strong	Medium	Medium to high	-10 < T < 1	V > 10	Days
Soft rime	200-600	Medium	Small	Low	-20 < T < 1	V < 10	Days

Given the degree of complexity in modeling icing effects on wind turbines, no general physical icing-loss model appears to have been developed to date in AWST's knowledge (DeGaetano et al. 2008, Pytlak et al. 2010, Nygaard et al. 2011, Yang et al. 2015). Therefore, AWST's pragmatic approach for this study was to create a conceptual model based on atmospheric conditions predicted by the WRF model, and then to tune its parameters to the estimated icing losses in the SCADA data for the 18 operational wind farms.

Based on the fundamentals of meteorology (Ahrens 2003) and a review of papers related to icing (Jones 1998, IEC 60826), it was concluded that rime icing is mostly influenced by cold temperatures and high humidity, whereas for precipitation icing the driving factors are cold temperatures and rainfall. In both cases, wind speed plays a secondary role.

Due to the complexity and non-linear interactions between those meteorological variables and the actual lost energy from icing, AWST built its icing model around a generalized additive model (GAM). A GAM is basically a sum of non-linear functions of each predictor variable. The challenge with GAM is to find suitable parametric representations for the non-linear functions, i.e. choose the degree of smoothness appropriately (James et al. 2013). The GAM uses the WRF model outputs as the predictors and the lost energy due to icing effects derived from the operational data as the predictand or dependent variable.

The icing model was built using non-linear relationships between the met variables (i.e. predictors) and the power generation (predictand) at the individual turbine level. It is also consistent with the way the OpenWind software simulates icing losses at the turbine level. GAMs are powerful tools to build statistical models but they can potentially overfit if left unchecked. In order to lower the risk of overfitting, the degrees of freedom for each predictor-predictand relationship must be kept low otherwise the non-linear functions will show large fluctuations that are not realistic. Upon visual inspection of the non-linear functions determined by the GAM, it was found that the behavior tends to follow common physical sense, but not at all times. For instance,

[4.7] Taken from the IEC 60826.

the non-linear function in the GAM shows an increase in icing loss as the cumulative precipitation increase until the cumulative precipitation reaches 300-400 mm. Above that threshold, the icing loss was decreasing with increasing cumulative precipitation which is not realistic. It appears that the GAM was overfitting when the sample size is low in some parts of the predictor domain (such as very high cumulative precipitations). To remedy this situation, a more intuitive icing model heavily inspired by the GAM was custom designed for this project. The goal was to retain the main features of the non-linear functions developed by the GAM while manually adjusting the behavior of those non-linear functions when the predictor domain has a low sample size. Internal validation shows the GAM outperforms the custom icing model by less than 5% in RMSE. The validation was performed using a 5-fold cross-validation to easily diagnose any overfitting. In the end, it was deemed to be a small price to pay in terms of accuracy compared to the risk of overfitting with the GAM.

4.3.4 Environmental - temperature shutdown

Turbine shutdowns can be triggered by very low or very high temperatures. Temperature shutdown losses vary with climate, of course, but for most wind farms in the mid-latitudes these energy losses are typically below 1% on an annual average. During the winter, turbines equipped with a cold weather package can safely operate down to -30°C. Every wind farm under contract with HQD has the cold weather package included on their turbines. The coldest temperature recorded by any of the met masts used in the project was -35°C. In warm weather, turbines can operate to temperatures of at least 35°C. The temperatures in Québec very rarely reach such highs. The highest recorded temperature by the met masts was 41°C.

Openwind models the low- and high-temperature shutdown behavior for each turbine type. The turbine characteristic files which serve as inputs to the Openwind software include several wind turbine control set points such as the minimum and maximum threshold for temperature shutdowns and power curve derating if applicable.

4.3.5 High Wind Hysteresis

Wind turbines typically cut out under sustained wind speeds averaging about 22 to 25 m/s over 10-minute period depending on the turbine model.[4.8] Once the turbine is shut down due to high winds, it is brought back online only after wind speeds have typically dropped by 3 m/s from the cut-out wind speed. This type of wind energy loss is called high wind hysteresis. This behavior is modeled in Openwind based on the turbine characteristic files, which include the cut-in, cut-out and cut-back-in wind speed information for each turbine model as well as the power curve derating (i.e. storm control system) if applicable.

[4.8] The turbine is switched off and their blades feathered to minimize loads.

4.3.6 Turbine Performance

Turbines can underperform for a variety of reasons.[4.9] They include incorrect turbine control settings, as well as high turbulence, shear, or inclined flow departing from the conditions for which the power curve has been defined.[4.10] These losses individually tend to be small but can be significant depending on site conditions. In addition, there is evidence that turbines often fall short of their advertised power curves even in IEC-compliant power curve tests. A review of IEC-compliant power performance tests indicates that turbines fall below their advertised power curves by an average of 2.4% (Bernadett et al. 2012).

For this study, we introduced a general turbine performance loss of approximately 2.4% by applying a power curve adjustment in the Openwind simulations. The loss is applied as an effective speed penalty.

4.3.7 Electrical Losses

Electrical losses are experienced by all electrical components of a wind farm, including the padmount and substation transformers, electrical collection system as well as the power consumption of cold weather packages and de-icing systems.

4.3.7.1 Electrical Efficiency

The electrical efficiency of a wind farm is primarily driven by losses associated with the transformers and the collector system. It appears as a difference between the sum of individual turbine energy output measured at each padmount transformer, and the power measured at the revenue meter on the high-voltage side of the substation as it passes into the HQD grid. This source of loss was estimated by comparing the revenue-meter production and recorded turbine production in the SCADA data for each plant. Electrical efficiency losses are typically between 2% and 3%. Figure 4.3 shows that when the gross wind power generation is approximately 15% or more of the plant capacity, the electrical losses are slightly below 2% of the gross power output, and rises only very slightly with increasing generation. The high losses when gross power output is below approximately 10% are driven primarily by the losses associated with the transformers rather than the electrical collection system. While air temperature could be a potential driver of electrical losses, the data did not show a statistically significant relationship. An electrical efficiency model similar to that shown in Figure 4.3 was implemented for each turbine model in Openwind.

[4.9] The turbine produces output below its nominal power curve.

[4.10] For instance, yaw misalignments, control anemometer calibration errors, and blade pitch inaccuracies or misalignments.

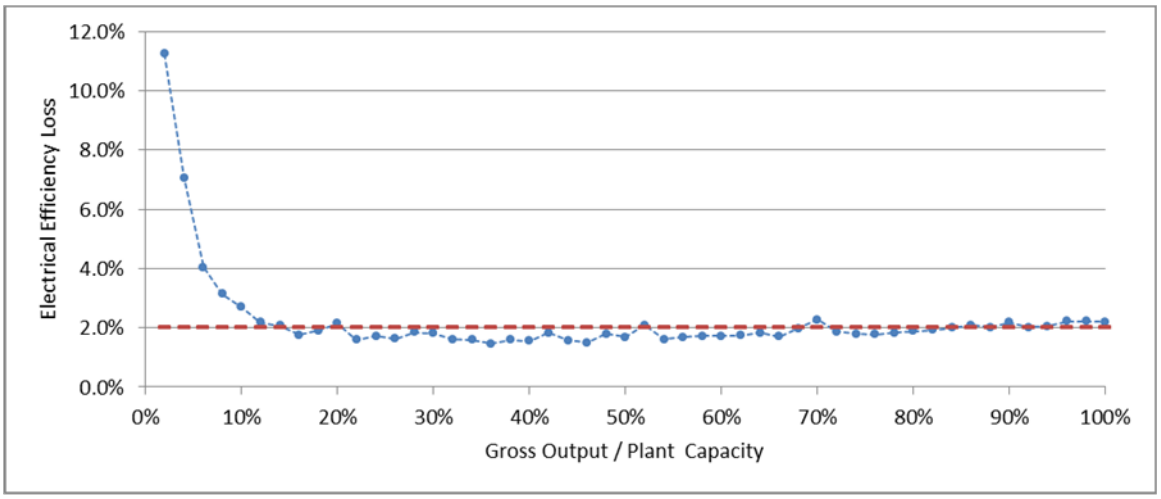

Figure 4.3: Average electrical efficiency loss as a function of gross energy output relative to plant capacity.

4.3.7.2 Turbine Power Consumption

Modern wind turbines consume power to run equipment such as yaw mechanisms, blade-pitch controls, aircraft warning lights, oil heaters, pumps, and coolers for the gearbox and hydraulic brakes for locking blades down in high winds, etc. The sum of these sources of turbine power consumption is typically much less than 1%, even for wind turbines equipped with a cold weather package. De-icing systems can consume more power, however. In order to estimate the electrical power consumption of the turbines, the turbine output is assessed while offline. At those times, the turbine power output is negative, meaning that it is a net consumer of electrical power. While it is not possible to estimate the power consumption of the cold weather packages separately, their power consumption is reflected in the increasing energy loss with colder temperatures.

AWST developed a separate module in Openwind for the RBHS. The goal was to simulate the reduction in icing losses due to the RBHS, as well as its power consumption. The RBHS module includes two main features: (a) a trigger function to automatically start the RBHS and (b) an efficiency parameter to simulate the rate of melting ice on the blades. The RBHS is not initiated under very light icing conditions. If the RBHS is activated, the melting rate is set to 0.75% per hour. This allows the simulated icing losses to gradually decrease with time. It is expected that the annual average power consumption for turbines equipped with a RBHS will remain in the 0% to 3% range in Québec.

4.4 Validation of Openwind Simulations at Operational Wind Farms

The primary goal of this project was to provide realistic wind power generation time series to HQD. The Openwind simulations were validated to ensure that they produce similar wind energy patterns as actually observed by the 18 operational wind farms with at least one year of SCADA data. Table 4.2 shows the average net production values and model bias, as well as hourly and daily correlations between the observed and modeled net power over the concurrent period for the 18 operational wind farms. Note that some wind farms have far more years of operation than

others, especially the wind farms with GE turbines. There is generally very strong agreement between the average observed and modeled net power, which is not surprising given that the WRF wind data were tuned to minimize the average bias between modeled and observed power. The coefficient of determination (R^2) of hourly and daily net power is a better indication of the quality of the WRF-WindMap-Openwind simulations. The hourly R^2 average 0.80, while the daily R^2 average 0.88 which indicate a strong correlation. The three wind farms with the lowest correlation, P11, P15 and P32, experience the most intense icing losses of all the operational wind plants in Québec. The monthly net power at P15, P32 (see Figure 4.5) and P11 (see Figure 4.8) clearly show that the modeled time series do not match with the observed data as well as the other plants.

Overall, the high correlation and low bias between modeled and observed values is evident in the monthly average net power plots in Figure 4.4 to Figure 4.9. Note, that the periods vary for each figure based on the duration of available SCADA data. Overall, the modeled net power time series track the observed values at all projects quite well. A visual inspection of Figure 4.5 to Figure 4.9 confirms that the Openwind simulations capture the seasonal trends in net power. The wind farms with the longest period of operational data, i.e. P1, P2 and P3, clearly show a seasonal pattern typical of Québec's climate with the lowest wind energy production during the summer season and highest production in the winter.

Table 4.2: Net power statistics at operational wind farms

Project	WindMap Domain	Number of Months	Observed net power (MW)	Modeled net power (MW)	Difference in net energy	Hourly R^2	Daily R^2
P33	A	36	29.70	29.80	0.1%	0.77	0.89
P32	B	24	28.97	28.69	-0.4%	0.72	0.78
P15	B	24	51.76	52.28	0.3%	0.75	0.80
P8	B	24	46.06	46.08	0%	0.83	0.89
P6	B	25	38.43	37.81	-0.6%	0.86	0.93
P26	C	25	46.04	45.33	-0.5%	0.83	0.90
P27	C	24	50.89	50.30	-0.4%	0.78	0.86
P37	D	24	8.68	8.63	-0.2%	0.81	0.91
P2	E	95	33.18	32.95	-0.2%	0.79	0.90
P14	E	45	40.72	40.47	-0.2%	0.86	0.92
P11	E	24	95.26	95.22	0%	0.75	0.79

Project	WindMap Domain	Number of Months	Observed net power (MW)	Modeled net power (MW)	Difference in net energy	Hourly R^2	Daily R^2
P34	E	72	38.21	37.84	-0.3%	0.84	0.92
P16	F	50	35.66	35.66	0%	0.76	0.84
P10	F	37	75.49	75.31	-0.1%	0.83	0.90
P18	F	48	22.07	22.10	0.1%	0.79	0.89
P1	F	87	33.29	33.63	0.3%	0.81	0.88
P22	F	33	20.97	21.02	0.1%	0.83	0.92
P3	F	85	38.25	37.98	-0.2%	0.81	0.88
AVERAGE	-	-	**40.76**	**40.62**	**-0.12%**	**0.80**	**0.88**
STDEV	-	-	**19.77**	**19.75**	**0.27%**	**0.04**	**0.05**

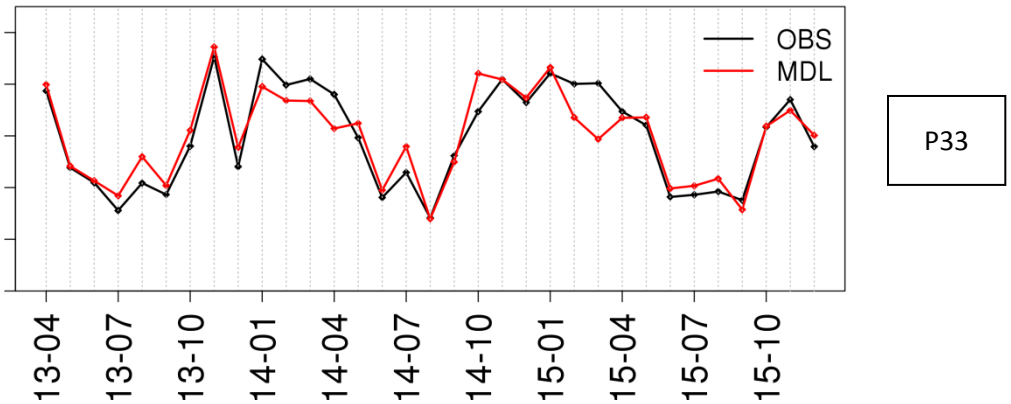

Figure 4.4: Monthly average observed (black) and modeled (red) net power for project –P33 in domain A.

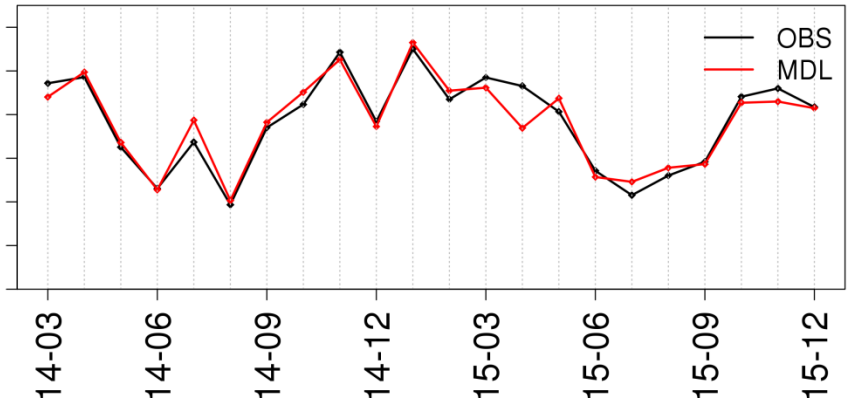
OBS
MDL
14-03
14-06
14-09
14-12
15-03
15-06
15-09
15-12

P6

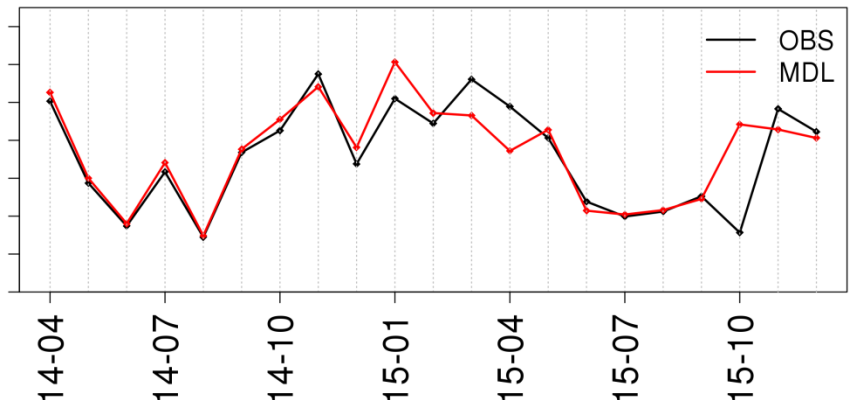
OBS
MDL
14-04
14-07
14-10
15-01
15-04
15-07
15-10

P8

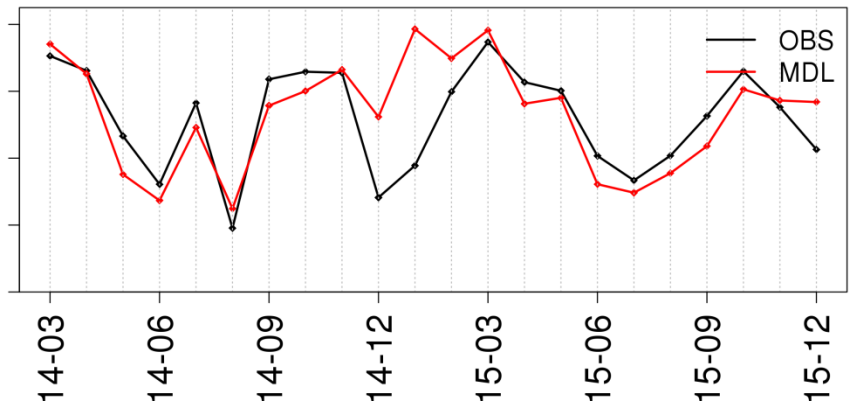
OBS
MDL
14-03
14-06
14-09
14-12
15-03
15-06
15-09
15-12

P15

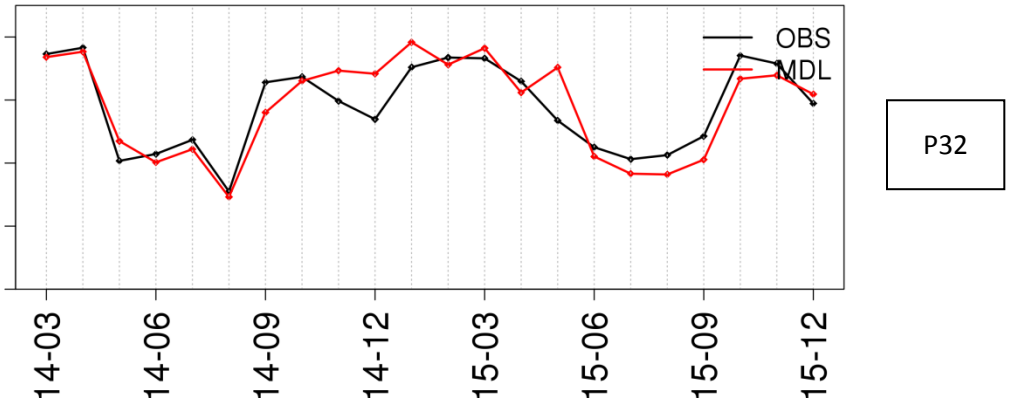

Figure 4.5: As in Figure 4.4 but for projects P6, P8, P15 and P32 in domain B.

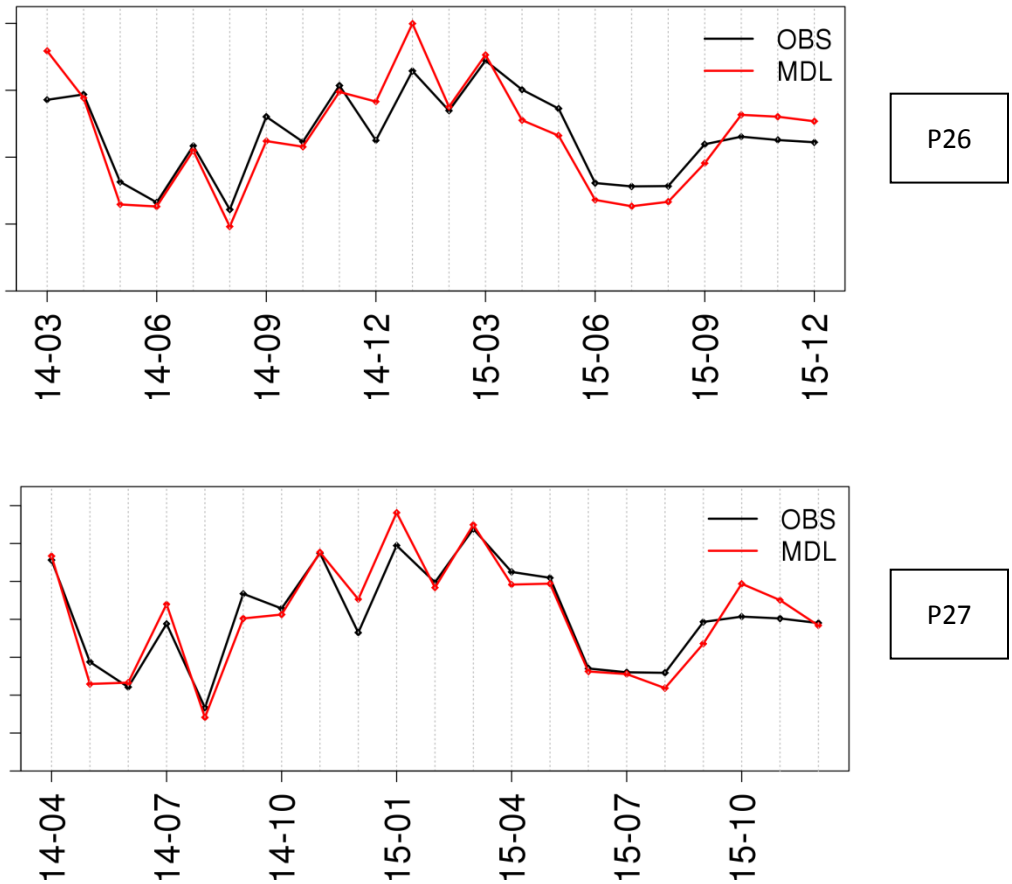

Figure 4.6: As in Figure 4.4 but for projects P26 and P27 in domain C.

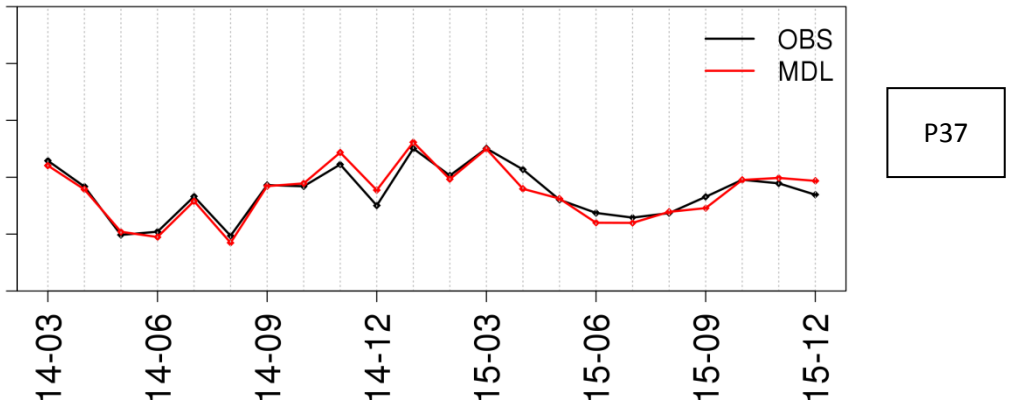

Figure 4.7: As in Figure 4.4 but for project P37 in domain D.

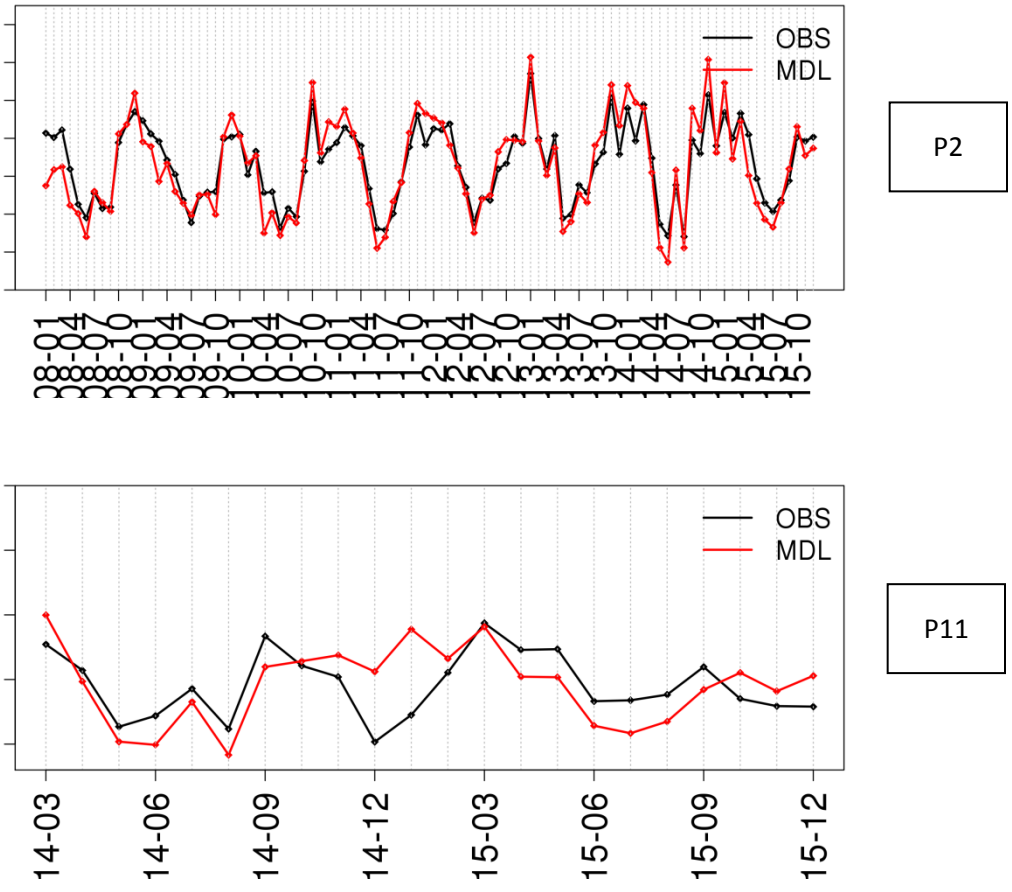

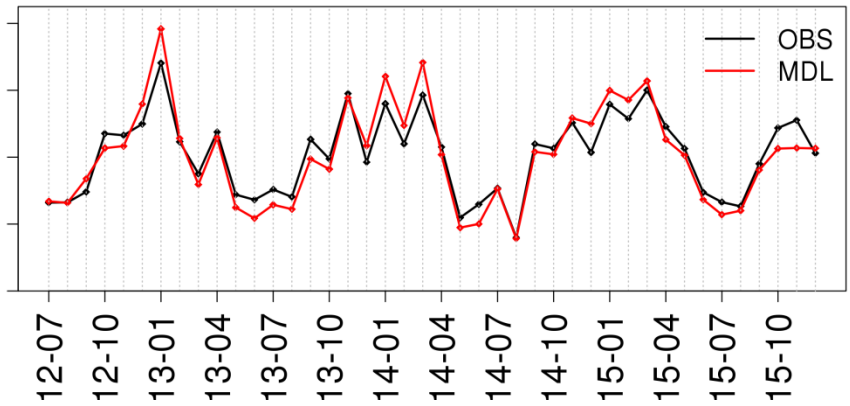

P14

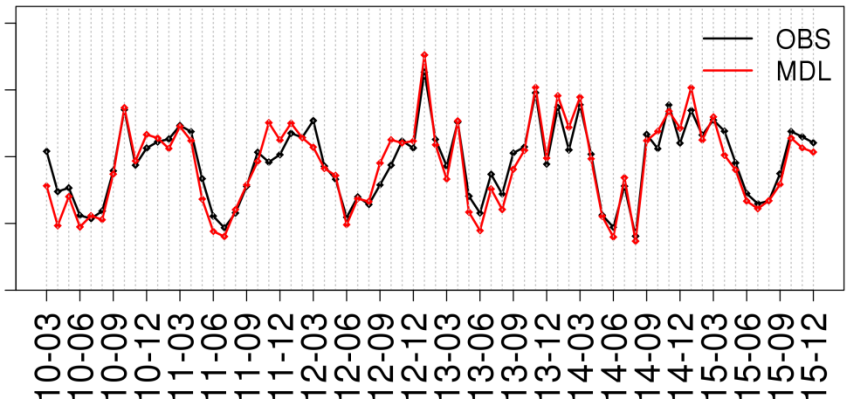

P34

Figure 4.8: As in Figure 4.4 but for projects P2, P11, P14 and P34 in domain E.

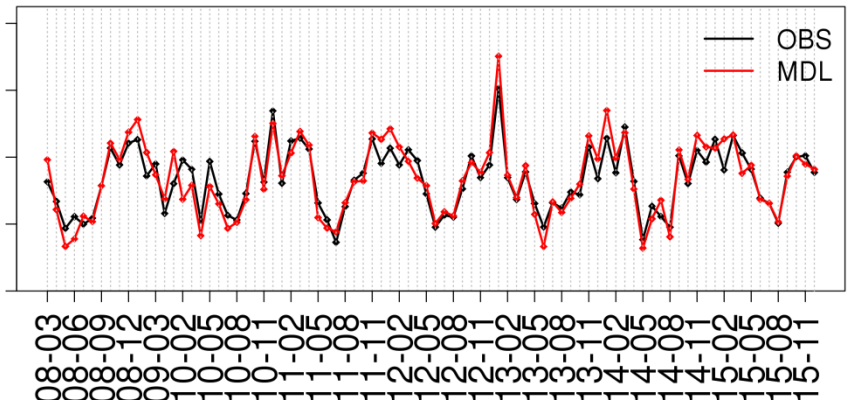

P1

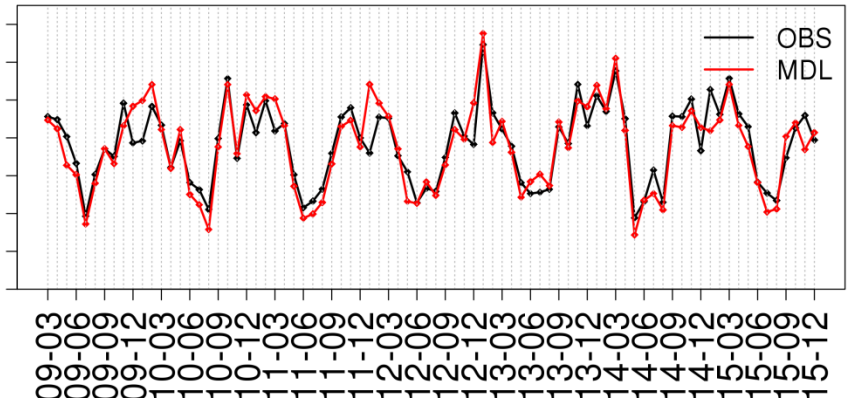
OBS
MDL
09-03
09-06
09-09
09-12
10-03
10-06
10-09
10-12
11-03
11-06
11-09
11-12
12-03
12-06
12-09
12-12
13-03
13-06
13-09
13-12
14-03
14-06
14-09
14-12
15-03
15-06
15-09
15-12

P3

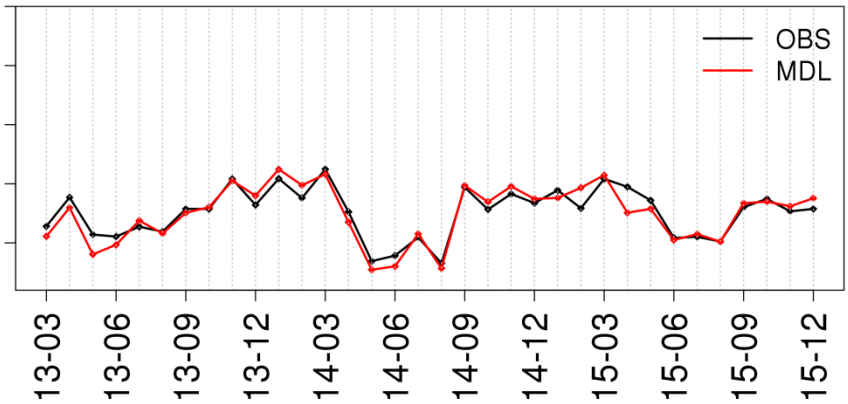
OBS
MDL
13-03
13-06
13-09
13-12
14-03
14-06
14-09
14-12
15-03
15-06
15-09
15-12

P10

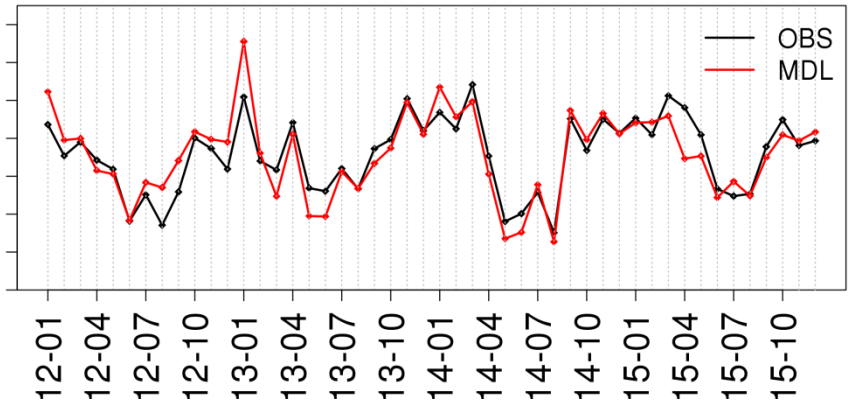
OBS
MDL
12-01
12-04
12-07
12-10
13-01
13-04
13-07
13-10
14-01
14-04
14-07
14-10
15-01
15-04
15-07
15-10

P16

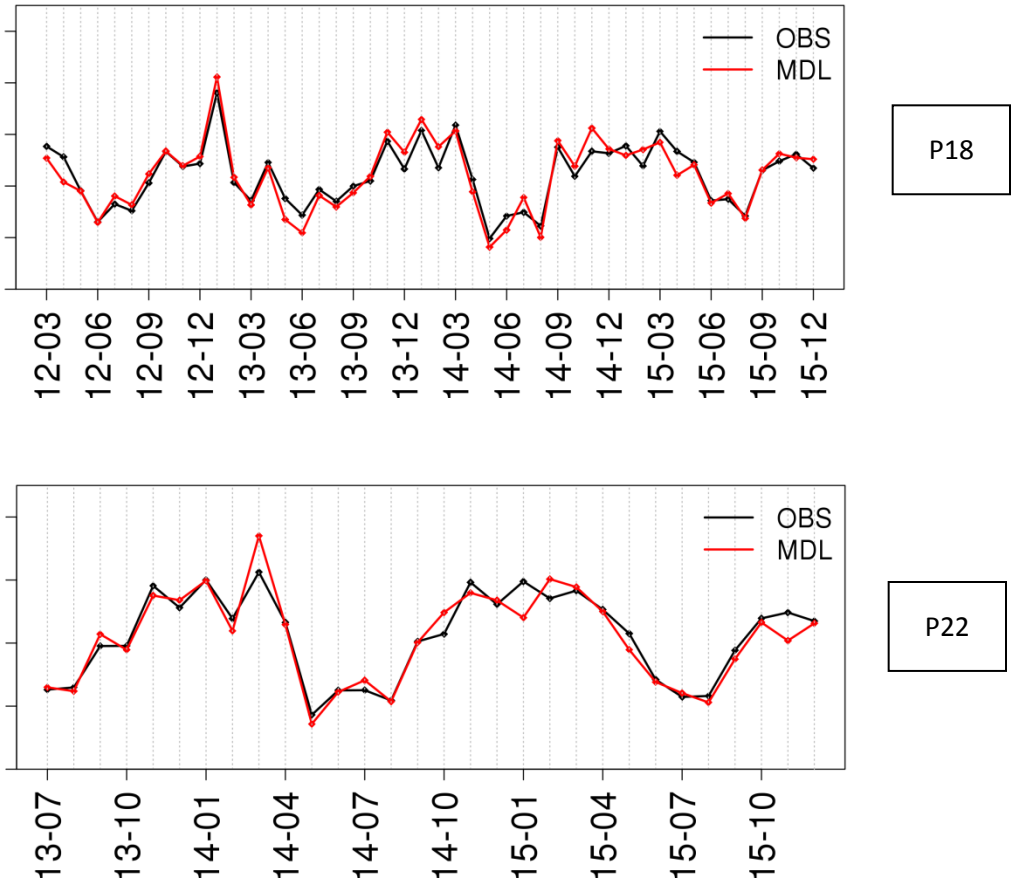

Figure 4.9: As in Figure 4.4 but for projects P1, P3, P10, P16, P18 and P22 in domain F.

Of the three largest categories of energy losses[4.11], two of them, availability and icing, can be estimated from the SCADA system at the operational wind farms. In order to provide a fair comparison between the observed and modeled plant losses, the plant losses related to Figure 4.10 and Figure 4.11 are reported relative to the gross power generation minus the wake losses because the observed gross power has the wake losses baked into it.[4.12]

The wind plant availability modeled by Openwind was tested against actual availability observations from the 18 operational wind farms. The bar plot in Figure 4.10 indicates the average modeled and observed availabilities at each operational wind farm are reasonable. The average modeled availability was 95.8% compared to an observed average availability of 95.5%, both numbers correspond to energy-weighted availability.[4.13] The P10 and P18 wind farms were left out

[4.11] Availability, wakes and icing losses

[4.12] The gross power at each turbine is estimated from the historical power curves, i.e. nacelle wind speed vs. turbine power generation.

[4.13] Arithmetic average

because of the particular settings of the SCADA system under low winds. The modeled availability losses are not as variable as the observed ones because a single set of seasonal transition matrices was used in the Openwind simulations for all wind farms.

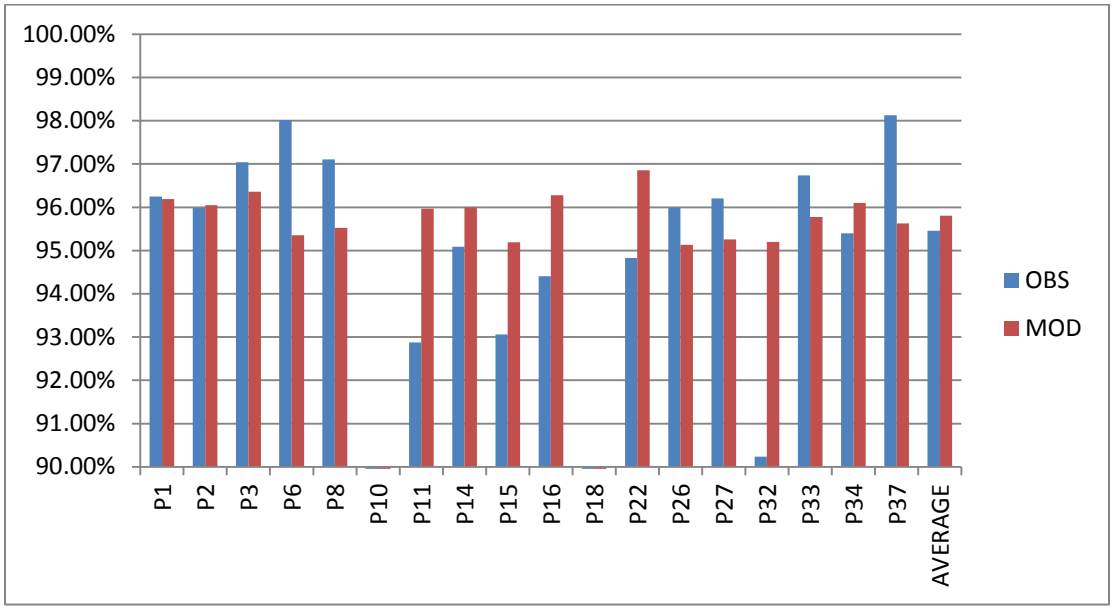

Figure 4.10: Comparison of observed (blue) and modeled (red) wind plant availability at the 18 operational wind farms over their concurrent period.

The observed and modeled icing losses at the 18 operational wind farms are presented in Figure 4.11. Results average around 4.1% and 4.6% respectively, indicating the Openwind simulations slightly overestimate the icing losses.[4.14] Recall from Section 4.1, AWST determines the actual icing losses at an operational wind farm using a similar approach as the IEA Task 19. Still, it is not a straightforward task to calculate icing losses from SCADA data. AWST's confidence in the observed icing loss values at the operating wind farms is not as high as the availability numbers. The Openwind simulations have larger errors related to icing losses at wind farms experiencing huge icing losses such as P11, P15 and P32. Wind farms with long periods of records, like P2 and P34 in Figure 4.8 or P1 and P3 in Figure 4.9, indicate that the net power generation modeled from the Openwind simulations fits similarly well during the winter months as for any other months.[4.15] It is also true for wind farms equipped with a RBHS. Thus it appears that the RBHS module in Openwind is working reasonably well.

[4.14] Arithmetic average

[4.15] Net energy peaks during the winter, trough in summer.

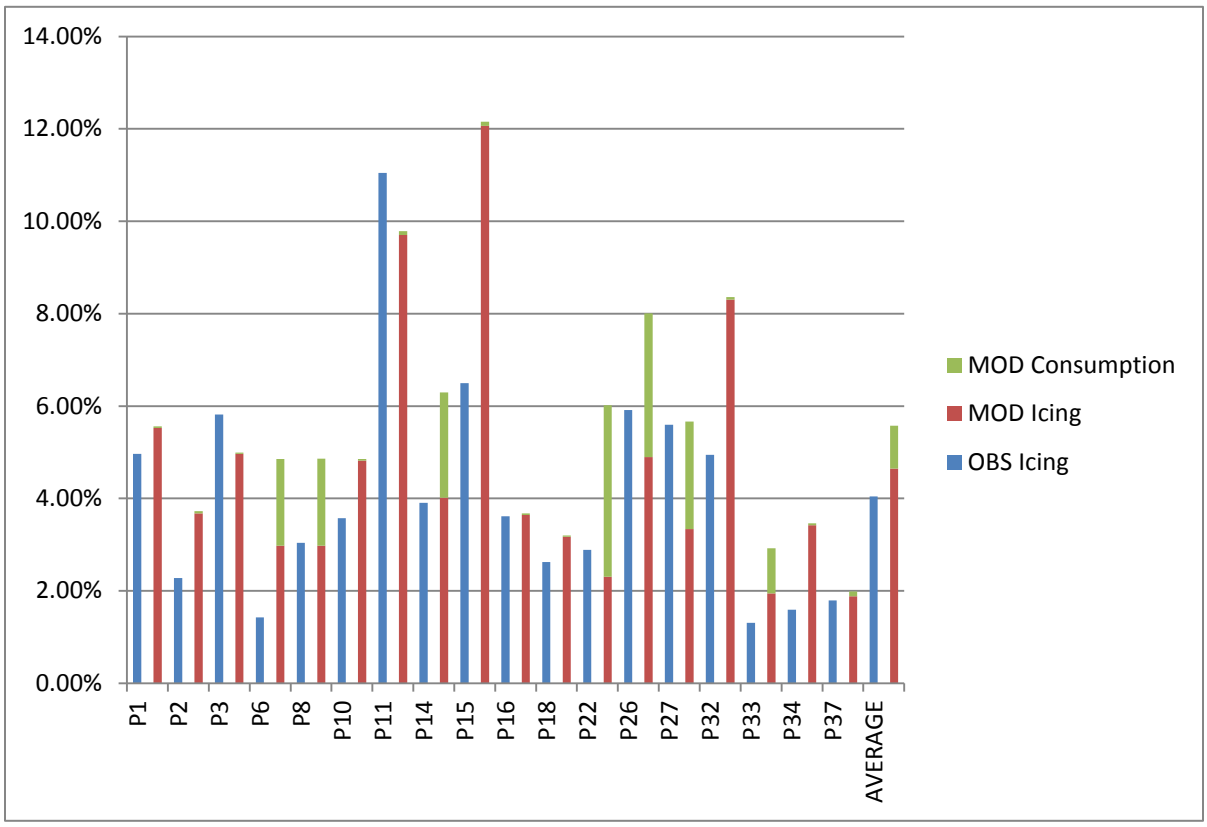

Figure 4.11: Comparison of observed (blue) and modeled (red) wind plant icing losses at the 18 operational wind farms over their concurrent period.

5. CONCLUSIONS

AWS Truepower (AWST) was retained by HQD to develop a historical simulation of wind power generation and associated losses for the period of 1979 – 2015. AWST's primary objective in this project was to create realistic long-term wind power time series that mimic the operational behavior of the 39 existing and planned wind plants under contract with HQD to support HQD's analyses of the contribution of wind power plants to the power system. The Weather Research and Forecasting (WRF) model, a leading open-source community model, was used to generate the meteorological variables necessary to simulate wind energy production. The simulated wind speeds were further downscaled with the WindMap microscale model. The conversion of the hourly meteorological time series into wind power generation was carried by the Openwind software. Improvements in modeling time-varying plant losses allowed the Openwind software to simulate a wind plant as a fully dynamic system by reporting wind power generation and individual plant losses on an hourly basis. The categories of plant losses included: wakes, availability, environmental (low and high temperature shutdowns, high wind hysteresis, icing), turbine performance and electrical losses (electrical efficiency and turbine power consumption).

The modeled net power generation was compared to actual (observed) generation at each 18 operational wind farm. The validation of the WRF-WindMap-Openwind simulations indicated that the net wind power generation was well aligned with the actual generation where the average hourly coefficient of determination (R^2) was 0.80, while the mean daily R^2 was 0.88. Our analyses also indicated that the monthly/seasonal trends in net power are well captured by the simulation system. The long-term average plant losses at each wind farm over the entire 37-year period are summarized in the report. A direct comparison between modeled and observed plant losses was not possible for this effort as most plant losses such as wakes and turbine performance are not easily derived from operational wind turbine data obtained through the SCADA system. Therefore, AWST's validation focused on the availability and icing losses which provided a reasonable approximation of the observed losses, although icing losses remain challenging at any given site. Power consumption losses, due to the rotor blade heating systems, were also a focal point. This report presents an overview of the methods, results, and validation of the historical wind power generation and associated plant losses at 39 wind farms in Québec.

REFERENCES

Ainslie, J. F. (1988). “Calculating the flowfield in the wake of wind turbines”, Journal of Wind Engineering and Industrial Aerodynamics, vol. 27, pp. 213-224

Ahrens, C.D. (2003). “Meteorology Today: An Introduction to Weather, Climate, and the Environment”, Broks/Cole, 7th edition, 545 pp.

AWS Truepower (2010). “Openwind – Theoretical Basis and Validation”, Version 1.3, Technical report from AWS Truepower, Albany (NY), USA. 26 pp. https://www.awstruepower.com/assets/OpenwindTheoryAndValidation_v1p3_Apr2010.pdf

Beaucage, P., M.C. Brower, J. Tensen (2014). “Evaluation of four numerical wind flow models for wind resource mapping”. Wind Energy, vol. 17, pp. 197-208.

Bendel, W.B and D. Paton (1981). “A Review of the Effect of Ice Storms on the Power Industry”. J. Appl. Meteor., vol. 20, pp. 1445–1449.

Bernadett, D., M. Brower, S. Van Kempen, W. Wilson, B. Kramak (2012). “2012 backcast study – verifying AWS Truepower’s energy and uncertainty estimates”. Technical report from AWS Truepower, Albany (NY), USA. 9 pp.

Brower, M.C. (1999). “Validation of the WindMap Program and Development of MesoMap”. Proceeding from AWEA's WindPower conference. Washington, DC, USA.

Brower, M.C. et al. (2012). “Wind Resource Assessment: A Practical Guide to Developing a Wind Project”. Wiley, 296 pp.

Brower, M.C., M.S. Barton, L. Lledo, and J. Dubois (2013). “A study of wind speed variability using global reanalysis data”. Technical report from AWS Truepower. 11 pp. Available at: https://www.awstruepower.com/knowledge-center/technical-papers/

Brower, M. C. and N. M. Robinson, (2012) “The Openwind Deep Array Wake Model – Development and Validation”, Technical report from AWS Truepower, Albany (NY), USA. 16 pp.

Crespo, A., J. Hernandez and S. Frandsen (1999). "Survey of modelling methods for wind turbine wakes and wind farms". Wind Energy, vol. 2, pp. 1-24.

Decker, M., M.A. Brunke, Z. Wang, K. Sakaguchi, X. Zeng, and M.G. Bosilovich (2012). “Evaluation of the Reanalysis Products from GSFC, NCEP, and ECMWF Using Flux Tower Observations”. Journal of Climate, Vol. 25, pp. 1916-1944

Dee, D. P., and Coauthors (2011). "The ERA-Interim reanalysis: configuration and performance of the data assimilation system". Q.J.R. Meteorol. Soc., vol. 137, pp. 553–597

DeGaetano, A.T., B.N. Belcher, and P.L. Spier (2008). “Short-Term Ice Accretion Forecasts for Electric Utilities Using the Weather Research and Forecasting Model and a Modified Precipitation-Type Algorithm”. Wea. Forecasting, vol. 23, pp. 838–853.

Frandsen, S.T. (2007). "Turbulence and Turbulence-Generated Structural Loading in Wind Turbine Clusters". Technical report from the DTU Wind Energy (Risø-R-1188), Roskilde, Denmark. 130 pp.

Frank, H.P. and L. Landbergh (1997). "Modeling the wind climate of Ireland". Boundary Layer Meteorology, vol. 85, pp. 359-378.

Garcia-Diez et al. (2013). “Seasonal dependence of WRF model biases and sensitivity to PBL schemes over Europe“, Q. J. R. Meteorol. Soc., vol. 139, pp. 501-514

IEC 60826 (2003). “Design criteria of overhead transmission lines”, 3rd edition. 243 pp.

IEC 61400-12-1 (2005). “Power performance measurements of electricity producing wind turbines”, 1st edition, 90 pp.

IEC 61400-26-2 (2014). “Production-based availability for wind turbines”, 1st edition, 47 pp.

International Electrotechnical Commission 61400-1 (2005). “Wind turbines – Part 1: Design requirements”, 3rd edition, 85 pp.

ISO 12494 (2001). “Atmospheric icing of structures”, 1st edition, 56 pp.

James, G., D. Witten, T. Hastie and R. Tibshirani (2013). “An introduction to statistical learning – with applications in R”, Springer, 426 pp.

Jensen, N.O. (1983) "A note on wind generator interaction". Technical report from the Risø National Laboratory (Risø-M-2411), Roskilde, Denmark. 16 p.

Jones, K.F. (1998). “A simple model for freezing rain ice loads”. Atmospheric Research, vol. 46, pp. 87–97

Kalnay, E., and Coauthors (1996). "The NCEP-NCAR 40-year reanalysis project". Bulletin of the American Meteorological Society, vol. 77, pp. 437–471

Lileo, S. and O. Petrik (2011). “Investigation on the use of NCEP/NCAR, MERRA and NCEP/CFSR reanalysis data in wind resource analysis”. Presentation given at the EWEA conference, Brussels, Belgium

Nygaard, B.E.K., J.E. Kristjánsson, and L. Makkonen (2011). “Prediction of In-Cloud Icing Conditions at Ground Level Using the WRF Model”. J. Appl. Meteor. Climatol., vol. 50, pp. 2445–2459.

Poulos, G. and V. Kumar (2013). “Investigating the Wind Flow Modeling Experiment”. Presentation given at the AWEA WRA workshop, Las Vegas (NV), USA

Pytlak, P., P. Musilek, E. Lozowski, and D. Arnold (2010). “Evolutionary Optimization of an Ice Accretion Forecasting System”. Mon. Wea. Rev., vol. 138, pp. 2913–2929.

Rienecker, M. M., and Coauthors (2011). "MERRA: NASA’s Modern-Era Retrospective Analysis for Research and Applications". J. Climate, vol. 24, pp. 3624–3648

Saha, S., and Coauthors (2010). "The NCEP Climate Forecast System Reanalysis. Bull. Amer. Meteor. Soc., vol. 91,pp. 1015–1057

Savadjiev and M. Farzaneh (2001). “Study of icing rate and related meteorological parameter distributions during atmospheric icing events”. Proceedings of the 11th International Offshore and Polar Engineering Conference, Stavanger, Norway, pp. 665-670.

Schlez, W. and A. Neubert (2009). "New Developments in Large Wind Farm Modeling". Proceedings from the EWEA conference 2009, Marseille, France. 8 p.

Skamarock, W. C. (2004). “Evaluating Mesoscale NWP Models Using Kinetic Energy Spectra”. Mon. Wea. Rev., vol. 132, pp. 3019-3032

Stull, R.B. (1988). “An introduction to boundary layer meteorology”, Kluwer Academic Publishers, 666 pp.

Troen, I. and E.L. Petersen (1989). "European Wind Atlas". Report from the Risoe National Laboratory, Roskilde, Denmark.

Vermeer, L.J., J.N. Sørensen and A. Crespo (2003). "Wind turbine wake aerodynamics". Progress in Aerospace Sciences, vol. 39, pp. 467-510.

von Storch, H. Langenberg, and F. Feser (2000). “A spectral nudging technique for dynamical downscaling purposes”. Mon. Wea. Rev., vol. 128, pp. 3664-2673

Yang, J., W. Yu, J. Choisnard, A. Forcione, and S. Antic (2015). “Coupled Atmospheric–Ice Load Model for Evaluation of Wind Plant Power Loss”. J. Appl. Meteor. Climatol., vol. 54, pp. 1142–1161.

ANNEXE B :

ÉVALUATION DE LA CONTRIBUTION EN PUISSANCE DE LA PRODUCTION ÉOLIENNE SOUS CONTRAT AVEC HYDRO-QUÉBEC DISTRIBUTION

Hydro Québec
Distribution

ÉVALUATION DE LA CONTRIBUTION EN PUISSANCE DE LA PRODUCTION ÉOLIENNE SOUS CONTRAT AVEC HYDRO-QUÉBEC DISTRIBUTION

Avril 2019

TABLE DES MATIÈRES

LISTE DES FIGURES ET TABLEAUX

1. INTRODUCTION

Cette étude vise à mettre à jour l'estimation de la contribution en puissance de la production éolienne sous contrat avec Hydro-Québec Distribution (le Distributeur). L'étude précédente, réalisée en 2009 et présentée à la Régie, se basait sur les séries historiques de production éolienne reconstituées par la firme Hélimax Énergie Inc. (Hélimax) (réf [1]). La mise à jour présentée ici repose sur les séries historiques de production reconstituées en 2016 par la firme AWS Truepower (AWS) (réf [2]) et qui intègrent, pour les parcs en opération, les observations collectées depuis leur mise en service.

Le présent rapport résume d'abord les données reconstituées de production découlant du mandat réalisé par AWS et présente ensuite la démarche utilisée pour réviser la contribution en puissance des éoliennes et, finalement, les résultats obtenus. Ces résultats sont utilisés pour établir la valeur à intégrer comme contribution en puissance à la pointe des éoliennes dans les exercices d'évaluation de la fiabilité en puissance de la zone d'équilibrage Québec.

2. DONNÉES DE PRODUCTION ÉOLIENNE

2.1. Reconstitution de séries de données historiques

La réalisation de diverses études d'impact de la production éolienne requiert des séries chronologiques de production. Les séries reconstituées en 2009 par Hélimax ont été réalisées à l'aide d'un modèle diagnostique CALMET[1]. Toutefois, aucune donnée réelle représentant la production des parcs éoliens sous contrat n'avait été utilisée pour cette modélisation.

Depuis 2006, plusieurs parcs éoliens sous contrat avec le Distributeur ont été mis en service. Certains parcs cumulent donc plusieurs années d'opération, permettant ainsi le développement de nouvelles séries intégrant les observations collectées depuis leur mise en service. La mise à jour des séries de production permet ainsi de tirer profit d'un historique climatique élargi, de nouvelles techniques de reconstitution de séries chronologiques de production éolienne ainsi que de la disponibilité des données météorologiques et d'opération des parcs mis en service.

Dans ce contexte, le Distributeur a mandaté AWS pour réaliser la reconstitution des séries historiques de production horaire pour les 39 parcs éoliens sous contrat avec lui, tels que connus en date de l'étude en 2015, et représentant une puissance installée totale de 3 710 MW.

À l'aide d'un modèle atmosphérique *Weather research and Forecasting* (WRF) – WindMap, la production éolienne a été simulée à l'emplacement des parcs éoliens en utilisant des

[1] CALMET est le module météorologique du modèle CALPUFF (www.src.com/calpuff/calpuff1.htm).

données météorologiques historiques couvrant la période de janvier 1979 à décembre 2015. Les séries de production reconstituées résultantes ont été validées et ajustées avec les données météorologiques et d'opération disponibles pour les parcs éoliens. Ainsi, les données réelles, provenant des 21 parcs en opération en 2015, ont été intégrées au modèle de reconstitution.

Le tableau 1 compare les principales caractéristiques du modèle développé par AWS à celles du modèle d'Hélimax, dont les résultats avaient été utilisés dans l'étude de l'évaluation de la contribution en puissance des éoliennes déposée en 2009. Ces informations permettent d'illustrer les améliorations amenées par les plus récentes simulations.

TABLEAU 1:
CARACTÉRISTIQUES DES MODÈLES ET DES INTRANTS – SÉRIES HÉLIMAX ET AWS

	Simulations Hélimax (2009)	Simulations AWS (2016)
Modèle utilisé	Modèle diagnostique CALMET (modèle 2D)	Modèle pronostique de méso-échelle WRF (modèle 3D) et le modèle micro-échelle WindMap
Parcs éoliens considérés dans la modélisation	Parcs éoliens A/O 2003 et 2005	Parcs éoliens A/O 2003, 2005, 2009, 2013 et parc Mesgi'g Ugiu's'n
Période modélisée	1971 à 2006	1979 à 2015
Données réelles d'opération d'un parc utilisées	Non	Oui
Données d'entrées des simulations	• Les données météorologiques horaires simulées par le modèle CALMET • Les courbes de puissance • Les configurations pré-construction des parcs éoliens	• Les données météorologiques horaires simulées par le modèle WRF/WindMap • Les courbes de puissance • Les configurations pré-construction des parcs éoliens pour les parcs non opérationnels • Les configurations des parcs éoliens tels que construits pour les parcs en opération
Pertes de production	Les pertes ont été modélisées selon les connaissances de l'industrie et l'expérience d'Hélimax en 2009	Les pertes ont été modélisées en utilisant les **données SCADA des éoliennes en opération** et selon les connaissances de l'industrie et l'expérience d'AWS
Données météorologiques simulées	• **Une** position (point) par parc. • Variables météorologiques simulées **à hauteur de moyeu** de l'éolienne • Résolution horizontale de 5 km	• **Plusieurs positions** (points) par parc • Variables météorologiques simulées **à plusieurs niveaux** (dont la hauteur de moyeu de l'éolienne) • Résolution horizontale de 2,5 km

Les informations concernant la localisation des parcs éoliens sous contrat avec le Distributeur sont présentées dans le tableau A1 en annexe.

2.2. Profils mensuels de production: comparaison des séries AWS et Hélimax

Les profils mensuels de production, exprimés par le facteur d'utilisation (FU), pour les séries reconstituées par AWS et Hélimax présentent des caractéristiques similaires, avec une production éolienne plus élevée durant les mois d'hiver et plus faible durant les mois d'été. La figure 1 compare les profils mensuels découlant des deux séries reconstituées, pour la période allant de janvier 1979 à décembre 2006[2] et pour les mêmes parcs éoliens. Pour la période d'hiver (de décembre à mars), le FU moyen est de 41,5 % pour les séries AWS et de 38,2 % pour les séries Hélimax.

FIGURE 1 :
COMPARAISON DU FACTEUR D'UTILISATION
POUR LA PÉRIODE 1979-2006 ENTRE LES SÉRIES AWS ET HÉLIMAX

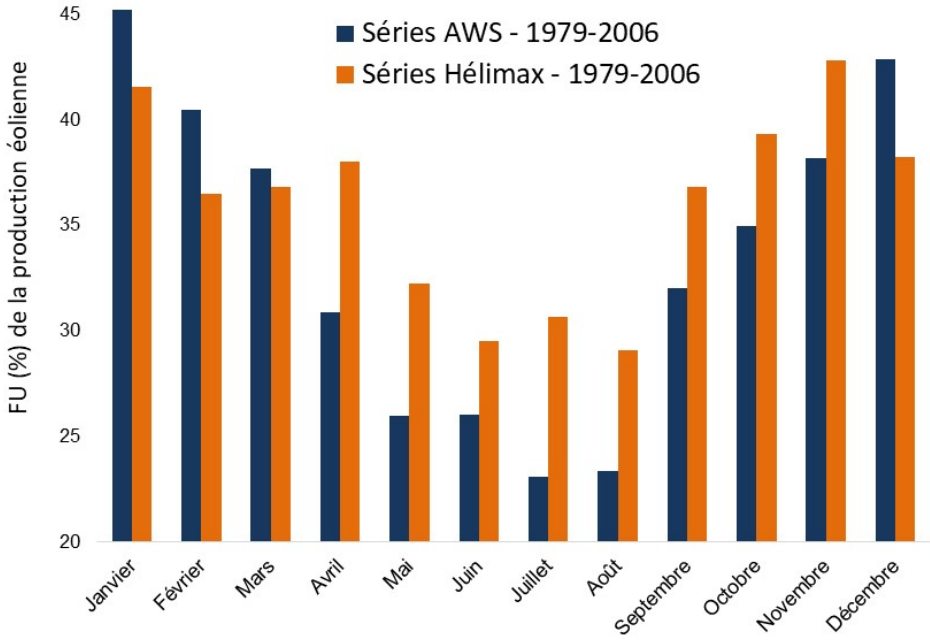

Comme mentionné précédemment, les séries reconstituées par AWS sont basées sur une méthodologie plus robuste, qui prend en compte une modélisation météorologique plus détaillée, ainsi que sur des données météorologiques et d'opération des parcs éoliens. Il s'agit donc d'une représentation de la production des parcs sous contrat avec le Distributeur qui intègre mieux la réalité opérationnelle et reflète l'intégration de nouvelles technologies éoliennes qui permettent d'en améliorer les performances, notamment par temps froid.

Il est à noter que, en utilisant les séries complètes d'AWS sur la période de 1979 à 2015, le facteur d'utilisation moyen calculé pour la période d'hiver est de 42,7 %.

[2] Il s'agit de la période commune couverte par les séries AWS et Hélimax.

3. MÉTHODOLOGIE UTILISÉE POUR ESTIMER LA CONTRIBUTION EN PUISSANCE À LA POINTE

Comme pour l'étude de 2009, le Distributeur a utilisé une variante de la méthode *Effective Load Carrying Capability* (ELCC) pour évaluer la contribution en puissance des éoliennes (réf [1], page 4). Cette méthode consiste à établir une équivalence entre, d'une part, l'apport d'un achat ferme et, d'autre part, celui d'un équipement éolien. Elle s'apparente à celles utilisées dans différentes études et par plusieurs juridictions nord-américaines et européennes.

Le Distributeur a utilisé le modèle de simulation *Multi Area Reliability Simulation* (MARS) pour appliquer la méthode ELCC. Il s'agit d'un modèle développé par General Electric, et utilisé par le Distributeur et les juridictions voisines, notamment les zones d'équilibrage du *Northeast Power Coordinating Council* (NPCC), afin d'évaluer la fiabilité de leurs approvisionnements.

3.1. Démarche de modélisation

La démarche suivie pour l'évaluation de la contribution des éoliennes comporte les deux étapes suivantes :

Étape 1 : Une première simulation inclut la charge, les ressources prévues dans le bilan en puissance et les 3 710 MW de production éolienne. La quantité d'achats fermes de puissance est toutefois ajustée pour obtenir le niveau de fiabilité cible (espérance de délestage d'un jour par dix ans ou LOLE = 0,1).

Étape 2 : Dans une seconde simulation, la production éolienne est retirée et une quantité d'achats fermes de puissance additionnelle est ajoutée de manière à ce que la fiabilité soit ramenée au niveau cible.

La contribution en puissance à la pointe des éoliennes correspond à la quantité d'achats fermes de puissance additionnelle ajoutée à l'étape 2, par rapport à celle requise à l'étape 1. Cet ajout de puissance est divisé par la puissance éolienne installée (3 710 MW) pour obtenir un résultat exprimé en pourcentage.

4. UTILISATION DU MODÈLE MARS ET RÉSULTATS

La réalisation des simulations avec le modèle MARS a nécessité l'utilisation de l'information suivante :

- les données de production éolienne simulées reconstituées pour la période 1979-2015 ;
- les données de charge et les aléas qui s'y rapportent ;
- les ressources du Distributeur ;
- les achats d'électricité prévus pour respecter le critère de fiabilité ;

- les moyens de gestion de la demande en puissance ;
- les contraintes de transport.

4.1. Intrants utilisés dans le modèle MARS

Les intrants utilisés pour l'évaluation de la contribution éolienne avec le modèle MARS sont basés sur les données présentées dans l'État d'avancement 2018 du Plan d'approvisionnement 2017-2026 pour le prochain hiver, soit l'hiver 2019-2020 (réf [5], page 13). Un profil de charge déterministe, représentatif des conditions climatiques normales, est utilisé. Le modèle MARS tient compte de l'aléa global sur la demande (aléa combiné prévisionnel + climatique) par le biais d'un générateur de scénarios de type Monte Carlo. Les données concernant les équipements de production, les programmes de gestion de la demande et les contraintes de transport sont conformes à celles utilisées pour les exercices de fiabilité.

4.1.1. Utilisation des données éoliennes dans MARS

Le modèle MARS permet de modéliser les ressources renouvelables et variables en utilisant la distribution de probabilité de production de ces ressources. Cette distribution permet de bien représenter la série de production.

La distribution cumulative de la production éolienne a été établie à partir des données de production des mois d'hiver (décembre à mars) des séries reconstituées par AWS pour la période 1979-2015.

Il s'agit de la même approche utilisée par le Distributeur pour modéliser les petites centrales hydrauliques (PCH) dans son modèle de fiabilité[3].

4.2. Résultats du modèle MARS

Les résultats détaillés de la modélisation réalisée avec le modèle MARS pour les séries AWS sont présentés dans le tableau 2.

Conformément à l'approche générale décrite à la section 3.1, un premier scénario incluant la production éolienne est calibré de manière à ce que l'espérance de délestage s'établisse au niveau requis pour satisfaire le critère de fiabilité (LOLE = 0,1 jour par année). Un tel scénario requiert des achats additionnels de 370 MW. Lorsque la production éolienne est retirée, les achats additionnels requis s'élèvent à 1 712 MW, soit 1 342 MW de plus que dans le scénario avec la production éolienne. Il y a donc une équivalence entre la contribution en puissance des achats garantis additionnels de 1 342 MW et les 3 710 MW de production éolienne. On retient donc un ratio de contribution en puissance à la pointe de 36 %.

[3] Voir le Plan d'approvisionnement 2017-2026 ; réf [3], page 25.

TABLEAU 2 :
RÉSULTATS DÉTAILLÉS DU MODÈLE MARS – SÉRIES AWS

Résultats détaillés MARS		Simulation avec production éolienne	Remplacement de la production éolienne par achats fermes garantis	Différence
Besoins en pointe 2019-2020		38 660	38 660	
Ressources engagées		40 780		
Électricité patrimoniale	37 442			
Appel d'offres de long terme (A/O 2015-01)	500			
Contrats avec HQP - Base et Cyclable	600			
Puissance rappelée	200			
Cogénération à la biomasse	295			
Petites centrales hydrauliques	103			
Abaissement de tension	250			
Électricité interruptible	1 000			
Programme GDP Affaires	390			
Autres achat fermes		370	1 712	1 342
Puissance éolienne installée		3 710	0	3 710
Espérance de délestage (jour/an)		*0,1*	*0,1*	

Idem

1 342 ÷ 3 710 = 36%

5. CONCLUSION

La mise à jour de la contribution en puissance à la pointe de la production éolienne est basée sur la même approche que celle utilisée en 2009, soit l'utilisation de la méthode ELCC.

Les résultats obtenus permettent d'établir la contribution en puissance à la pointe des éoliennes à 36 % de la puissance installée. La contribution estimée est supérieure à la valeur estimée en 2009 avec les séries Hélimax. Ce résultat est en lien avec le facteur d'utilisation attendu en hiver, qui est plus élevé pour les séries AWS que pour les séries Hélimax. Ce rehaussement du facteur d'utilisation pour les séries AWS découle d'une méthodologie plus robuste, qui tient compte de paramètres météorologiques raffinés, des caractéristiques sur les parcs éoliens installés et de données de production réelle.

Sur la base des résultats obtenus avec le modèle MARS, le Distributeur retient une contribution en puissance à la pointe des éoliennes de 36 % de la puissance installée. Cette valeur sera notamment utilisée pour les évaluations de la fiabilité déposées auprès du NPCC pour la zone de réglage Québec.

RÉFÉRENCES

[1] Hydro-Québec Distribution, *Évaluation de la contribution en puissance de la production éolienne sous contrat avec Hydro-Québec Distribution,* octobre 2009, 18 pages : http://www.regie-energie.qc.ca/audiences/EtatApproHQD/Rapport_Contribution%20en%20puissance%20.pdf

[2] AWS Truepower, *Historical Meteorological and Wind Power Time Series 1979-2015*, December 2016, 53 pages

[3] Hydro-Québec Distribution. *Plan d'approvisionnement 2017-2026* (dossier R-3896-2016), pièce HQD-1, document 1 (B-0006), 1er novembre 2016 : http://publicsde.regie-energie.qc.ca/projets/389/DocPrj/R-3986-2016-B-0006-Demande-Piece-2016_11_01.pdf

[4] Hydro-Québec Distribution, *2017 Québec Area Comprehensive Review of Resource Adequacy - Approved by the RCC*, December 5, 2017, 32 pages: https://www.npcc.org/Library/Resource%20Adequacy/2017%20Quebec%20Comprehensive%20Review.pdf

[5] Hydro-Québec Distribution, *État d'avancement 2018 du Plan d'approvisionnement 2017-2026*, 1er novembre 2018, 57 pages: http://www.regie-energie.qc.ca/audiences/Suivis/SuiviD-2017-140_PlanAppro2017-2026/HQD_SuiviPlanAppro2017-2026_1nov2018.pdf

[6] C.J Dent, S. Zachary, *Capacity Value of Additional Generation: Probability Theory and Sampling Uncertainty*, *Proceedings of the Institution of Mechanical Engineers, Part O: Journal of Risk and Reliability*, 2013

[7] E. Ibanez and M. Miligan, *Impact of Transmission on Resource Adequacy in Systems with Wind and Solar Power*, Published in the 2012 IEEE Power and Energy Society General Meeting

[8] S. Maheswari, C. Vijayalakshmi, *Maximum Wind Power Penetration Using LR Technique*, *Applied Mathematical Sciences*, vol. 7, 2013, no. 23, 1135-1141

[9] S. Lu, R.Diao, N. Samaan, P. Etingov, *Capacity Value of PV and Wind Generation in the NV Energy System*, Prepared for the U.S Department of Energy, Pacific Northwest National Laboratory, September 2012

[10] M. Milligan, K. Porter, *Determining the Capacity Value of Wind: An Updated Survey of Methods and Implementation*, National Renewable energy Laboratory, June 2008.

ANNEXE :

LOCALISATION DES PARCS ÉOLIENS SOUS CONTRAT AVEC LE DISTRIBUTEUR

TABLEAU A1 :
LOCALISATION DES PARCS ÉOLIENS SOUS CONTRAT AVEC LE DISTRIBUTEUR[4]

Nom du projet	Région administrative	Région de transport où le projet est raccordé
1er Appel d'offres		
Parc éolien de Baie-des-Sables	Bas-Saint-Laurent	Québec Centre
Parc éolien de L'Anse-à-Valleau	Gaspésie–Îles-de-la-Madeleine	Québec Centre
Parc éolien de Carleton	Gaspésie–Îles-de-la-Madeleine	Québec Centre
Parc éolien de Saint-Ulric-Saint-Léandre	Bas-Saint-Laurent	Québec Centre
Parc éolien Mont-Louis	Gaspésie–Îles-de-la-Madeleine	Québec Centre
Parc éolien de Montagne Sèche	Gaspésie–Îles-de-la-Madeleine	Québec Centre
Parc éolien de Gros-Morne	Gaspésie–Îles-de-la-Madeleine	Québec Centre
2e Appel d'offres		
Parc éolien Le Plateau	Gaspésie–Îles-de-la-Madeleine	Québec Centre
Parc éolien de Saint-Robert-Bellarmin	Estrie	Nicolet Des Cantons
Parc éolien Montérégie	Montérégie	Montréal
Parc éolien du Massif du Sud	Chaudière-Appalaches	Québec Centre
Parc éolien du Lac-Alfred	Bas-Saint-Laurent	Québec Centre
Parc éolien de New Richmond	Gaspésie–Îles-de-la-Madeleine	Québec Centre
Parc éolien de L'Érable	Centre-du-Québec	Québec Centre
Parc éolien de la Seigneurie de Beaupré 2	Capitale-Nationale	Québec Centre
Parc éolien Des Moulins	Chaudière-Appalaches	Québec Centre
Parc éolien de la Seigneurie de Beaupré 3	Capitale-Nationale	Québec Centre
Parc éolien Des Moulins	Chaudière-Appalaches	Québec Centre
Parc éolien de la Seigneurie de Beaupré 4	Capitale-Nationale	Québec Centre
Parc éolien Vents du Kempt	Bas-Saint-Laurent	Québec Centre
Parc éolien de la Rivière-du-Moulin	Saguenay-Lac-Saint-Jean	Baie-James
Parc éolien Mont-Rothery	Gaspésie–Îles-de-la-Madeleine	Québec Centre
Parc éolien de Témiscouata 2	Bas-Saint-Laurent	Québec Centre
3e Appel d'offres		
Parc éolien Viger-Denonville	Bas-Saint-Laurent	Québec Centre
Parc éolien Le Granit	Estrie	Nicolet Des Cantons
Parc éolien de La Mitis	Bas-Saint-Laurent	Québec Centre
Parc éolien Le Plateau 2	Gaspésie–Îles-de-la-Madeleine	Québec Centre
Parc éolien de Saint-Damase	Bas-Saint-Laurent	Québec Centre
Parc éolien de Saint-Philémon	Chaudière-Appalaches	Québec Centre
Parc éolien de Témiscouata	Bas-Saint-Laurent	Québec Centre
Parc éolien Côte-de-Beaupré	Capitale-Nationale	Québec Centre
Parc éolien Frampton	Chaudière-Appalaches	Québec Centre
Parc éolien Pierre-De Saurel	Montérégie	Montréal
Parc éolien Des Cultures	Montérégie	Montréal
Parc éolien Belle-Rivière	Saguenay-Lac-Saint-Jean	Baie-James
4e Appel d'offres		
Parc éolien Roncevaux	Gaspésie–Îles-de-la-Madeleine	Québec Centre
Parc éolien Nicolas-Riou	Bas-Saint-Laurent	Québec Centre
Parc éolien Mont Sainte-Marguerite	Chaudière-Appalaches	Québec Centre
Contrat gré à gré		
Parc éolien Mesgi'g Ugju's'n	Gaspésie–Îles-de-la-Madeleine	Québec Centre

[4] La définition des régions de transport utilisée est identique à celle qui figure dans les attestations de fiabilité produites à la Régie de l'énergie et au NPCC. Voir à cet effet, la revue triennale produite pour la zone d'équilibrage du Québec (réf. [4] page 31).